






# Pol-InSAR and PolSAR based Inversion Modelling for Snow Depth and SWE Estimation in the Northwestern Himalayan Watershed

 Sayantan Majumdar<sup>a,b,\*</sup>,  Praveen K. Thakur<sup>b</sup>,  Ling Chang<sup>a</sup>,  
 Shashi Kumar<sup>b</sup>,  Sneh Mani<sup>c</sup>

<sup>a</sup>*Faculty of Geo-information Science and Earth Observation (ITC), University of Twente*

<sup>b</sup>*Indian Institute of Remote Sensing (IIRS), ISRO*

<sup>c</sup>*Snow and Avalanche Study Establishment (SASE), DRDO*


---

## Abstract

Snow depth (SD) and Snow Water Equivalent (SWE) constitute essential physical properties of snow and find extensive usage in the hydrological modelling domain. However, the prominent impact of the hydrometeorological conditions and difficult terrain conditions inhibit accurate measurement of the SD and SWE— an ongoing research problem in the cryosphere paradigm. In this context, spaceborne synthetic aperture radar (SAR) systems benefit from global coverage at sufficiently high spatial resolutions. The copolar phase difference (CPD) method based on the X-band polarimetric SAR (PolSAR) technique has displayed promising results regarding the fresh snow depth (FSD) estimation in the literature. Still, this FSD inversion model has not been tested in the presence of extreme topographically varying conditions, such as the northwestern Himalayan belt. It is also susceptible to high volume scattering at X-band occurring from the increased snow grain sizes as a result of the standing (or old) snow formation driven by the temperature induced snow metamorphosis process. Hence, to model this volume decorrelation, the polarimetric SAR interferometry (Pol-InSAR) technique can be applied. In this work, the FSD and standing snow depth (SSD) are computed using the

---

\*Corresponding author

Email address: [ir.sayantan.majumdar@gmail.com](mailto:ir.sayantan.majumdar@gmail.com) ( Sayantan Majumdar )

PolSAR CPD method and the single-baseline Pol-InSAR based hybrid Digital Elevation Model (DEM) differencing and coherence amplitude inversion model. To achieve these, the TerraSAR-X, TanDEM-X Coregistered Single look Slant range Complex (CoSSC) bistatic acquisition over Dhundi (situated in the Beas watershed, northwestern Himalayas, India) on January 8, 2016, is used. Due to the associated problems of model parameter tuning, complex topographical conditions, and limited ground-truth measurements, appropriate sensitivity analyses have been carried out for the parameter optimisation. Furthermore, the uncertainty sources are identified by performing a summer (June 8, 2017) and wintertime (January 8, 2016) comparative analysis of the study area which quantitatively highlights the changes in the percentages of the surface and volume scatterings. Evidently, the improved models display sufficiently high FSD and SSD accuracies of 94.83% and 99.53% respectively with the corresponding fresh SWE (FSWE) and standing SWE (SSWE) accuracies of 94.84% and 99.48% (measured using a  $3 \times 3$  window at Dhundi). These results demonstrate the practicability of the PolSAR and Pol-InSAR models in the context of the SD estimation over rugged terrains.

*Keywords:* Synthetic Aperture Radar, Copolar Phase Difference, Pol-InSAR, Snow Physical Properties, Sensitivity Analysis

---

## 1. Introduction

Snow depth (SD) and snow water equivalent (SWE) are two of the most important physical properties of snow and are extensively used in hydrological models that relate to snowmelt runoff and snow avalanche predictions (Thakur et al., 2017). While snow depth or snow height refers to the distance of the ground to the snow surface, SWE quantifies the amount of water present in a snowpack (layered snow formed by accumulation over time). Theoretically, SWE is defined as the product of snow depth and snow density and can be conceptualised as the amount of liquid water obtained owing to the instantaneous melting of an entire snowpack (Tedesco, 2015). Obtaining

accurate estimation of the SD and SWE is quite challenging depending upon the data availability, variety, and quality, parameterisation method, mathematical model selection, and the hydrometeorological conditions. Hence, it is considered to be an important research element in the cryosphere paradigm (Leinss et al.,  
15 2014, 2015, 2016; Conde et al., 2019).

Due to the difficulties posed by in-situ or ground based measurements of the SD and SWE in rugged terrains, remote sensing techniques coupled with adequately sampled (both in space and time domains) ground measurements are widely used to improve the quality of these estimated parameters over  
20 considerably large areas (Takala et al., 2011). Currently, LiDAR (Light Detection and Ranging) and spaceborne SAR (Synthetic Aperture Radar) are the most popular techniques used in the studies related to snow, ice and the cryosphere in general (Deems et al., 2013; Leinss et al., 2014; Tedesco, 2015). However, LiDAR can only be used to determine the height of the snow and  
25 cannot be used for measuring other physical properties such as snow density and snow wetness (Tedesco, 2015; Leinss et al., 2014). In addition, the operating cost of LiDAR is sufficiently high and is also weather dependent (Deems et al., 2013). As a result, spaceborne SAR systems benefit from substantial coverage (globally available), cloud insensitivity, all-day operability and are extensively used to  
30 measure the snow physical properties sufficiently at high spatial resolutions (Moreira et al., 2013; Thakur et al., 2012).

The applicability of SAR systems for snow cover monitoring was discussed as early as 1977 (Ulaby et al., 1977) wherein the snow backscatter coefficient was measured and was thereafter modelled for various frequencies, layers, and  
35 polarisations (Zuniga et al., 1979). It was shown that only very high microwave frequencies (Ku-band or higher) exhibit a significant dependence on SD or the SWE of dry or standing (deposited) snow (Yueh et al., 2009). However, lower frequencies (X-band or below) penetrate through dry snow whereby the underneath frozen soil or ground primarily contributes to the radar backscatter  
40 signal. Whereas, in case of moist snow (the transitional stage between dry and wet snow) and wet snow, the predominant scattering occurs from the snow

volume and snow surface respectively due to the presence of water. Essentially, water, with its high dielectric constant, heavily modifies the dielectric properties of snow and effectively reduces the snow penetration capacity of the radar pulses (Abe et al., 1990). The radar backscattering mechanism for a typical snow covered area can be conceptualised from Figure 1.1. In principle, PolSAR and InSAR systems utilise these received target echoes for supporting various microwave remote sensing applications in the cryosphere domain.

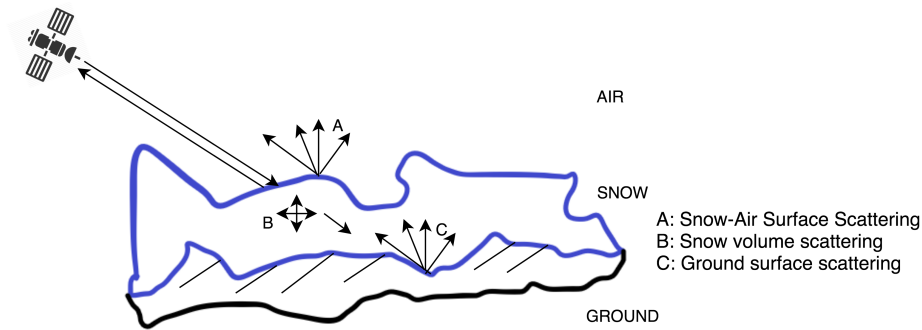


Figure 1.1: Conceptual diagram displaying the radar backscattering mechanism in hilly terrains. Adapted from [Thakur et al. \(2012\)](#).

PolSAR based algorithms which work on the polarimetric backscatter signal have been widely adopted for various snow related applications such as the classification of dry and wet snow, measuring snow wetness and snow density (Singh et al., 2017; Snehmami et al., 2010; Thakur et al., 2012, 2017; Usami et al., 2016). Leinss et al. (2014) introduced the use of spaceborne PolSAR for snow height determination, wherein the relationship between the copolar phase difference (CPD) and fresh snow depth (FSD) is quantitatively analysed by deriving a theoretical model (Leinss et al., 2014). Moreover, InSAR techniques find significant usage in the cryosphere domain and have been used to measure dry snow depth and SWE in several studies (Conde et al., 2019; Guneriussen et al., 2001; Leinss et al., 2015; Li et al., 2017; Liu et al., 2017). In this context, the Pol-InSAR technique works on the coherent combination of both PolSAR and InSAR observations, thereby enabling the interferogram generation

in arbitrary transmit and receive channels (Papathanassiou & Cloude, 2001; Cloude, 2005, 2010). It has been widely used for estimating tree height in forested regions and can be effectively applied to natural or artificial volume scatterers including snow and ice (Leinss et al., 2014; Hajnsek et al., 2009; Kugler et al., 2015; Kumar et al., 2017; Papathanassiou & Cloude, 2001).

The prime focus of this research is to estimate the FSD and SSD using PolSAR and Pol-InSAR respectively. Additionally, the corresponding fresh SWE (FSWE) and standing SWE (SSWE) are to be determined, for which the respective snow densities need to be known. In this work, the PolSAR CPD method (Leinss et al., 2014) is reproduced which shows high FSD and FSWE accuracies of 94.83% and 94.84% respectively. The main innovation lies in improving the Pol-InSAR based hybrid DEM differencing and coherence amplitude inversion model (Cloude, 2005, 2010). The SSD and SSWE results are estimated with accuracies of 99.53% and 99.48% respectively. These results are obtained after performing thorough sensitivity analysis of the free model parameters. Furthermore, the scattering characteristics of the study area are analysed using the dual-pol entropy ( $H$ ) and scattering angle ( $\alpha$ ) or  $H/\alpha$  decomposition, and unsupervised Wishart classification techniques (Lee & Pottier, 2009; Cloude, 2010; Singh et al., 2014) for identifying the potential uncertainty sources.

This manuscript is compartmentalised into five sections each consisting of several subsections. It starts with an introductory discussion in section 1. Thereafter, the methods involved in this work are described in section 2 following which the study area and the datasets including the required software are specified in section 3. The results are discussed in section 4. Finally, the relevant conclusions and recommendations are put forward in section 5.

## 2. Methodology

This section deals with the methodological framework which has been followed to generate the SD and SWE results. In order to briefly put the

overall workflow, a flowchart is shown in Figure 2.1 which highlights the main process blocks. Here, the preprocessing steps are discussed in section 2.1. Moreover, the PolSAR CPD and Pol-InSAR based approaches used for the FSD and SSD estimation respectively are individually addressed in sections 2.2 and 2.3. Finally, the uncertainty assessment, validation and sensitivity tasks are described in section 2.4.

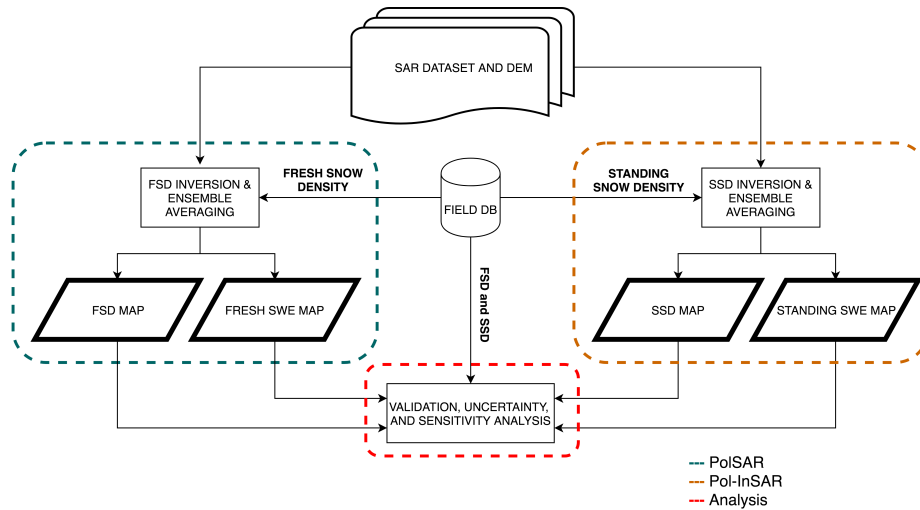


Figure 2.1: Overview of the main processing blocks.

### 2.1. Data Preprocessing

Since the SAR dataset is already coregistered, separate coregistration step has not been performed. In case of the FSD estimation model, the geocoded or terrain-corrected data (3 m spatial resolution) consists of the HH and VV scenes along with the local incidence angle (LIA) computed from the ALOS PALSAR DEM. As for the Pol-InSAR scenario, all the SAR channels, i.e., HH, HV, VH and VV along with the LIA are present in the geocoded data. It should be noted that, for the Pol-InSAR, processing both the master, TDX (master) and TSX (slave) images are required to generate the interferogram. However, the FSD estimation model can be used using any one of these images, though the

average of the TDX and TSX CPDs can potentially improve the signal-to-noise ratio (SNR) (Leinss et al., 2014).

## 2.2. CPD based Fresh Snow Depth Estimation

### 2.2.1. CPD Computation

The FSD is estimated using the CPD method developed by Leinss et al. (2014). At first,  $\phi_{CPD}$  for the TDX data ( $\phi_{CPD,TDX}$ ) acquired on January 8, 2016, is computed using Eq. (2.1a) and then an ensemble averaging operation is applied over a  $21 \times 21$  window (Majumdar et al., 2019). Similarly,  $\phi_{CPD}$  for the TSX data ( $\phi_{CPD,TSX}$ ) is calculated following which the average CPD,  $\overline{\phi_{CPD}}$  is obtained using Eq. (2.1b). Here,  $\Im$  and  $\Re$  denote the imaginary and real parts of the complex scattering matrices  $S_{VV}$  and  $S_{HH}$  respectively.

$$\phi_{CPD} = \phi_{VV} - \phi_{HH} = \left\langle \underbrace{\tan^{-1} \left( \frac{\Im(S_{VV})}{\Re(S_{VV})} \right)}_{\phi_{VV}} - \underbrace{\tan^{-1} \left( \frac{\Im(S_{HH})}{\Re(S_{HH})} \right)}_{\phi_{HH}} \right\rangle \quad (2.1a)$$

$$\overline{\phi_{CPD}} = \frac{\phi_{CPD,TDX} + \phi_{CPD,TSX}}{2} \quad (2.1b)$$

$\phi_{CPD}$  can be alternatively defined as the phase angle of the complex copolar coherence,  $\tilde{\gamma}_c$  (since  $\gamma$  is the standard notation for coherence amplitude,  $\tilde{\gamma}$  is used for the complex coherence), defined in Eq. (2.2). In this case, the copolar coherence amplitude ( $\gamma_c = |\tilde{\gamma}_c|$ ) is a measure of the radar backscattering mechanism where low values close to zero (ideally  $\gamma_c = 0$ ) indicate the presence of volume scattering and high values (ideally  $\gamma_c = 1$ ) represent surface scattering (Lee & Pottier, 2009; Leinss et al., 2014; Singh et al., 2014). It should be noted that only the CPD computed from side-looking radar systems is able to describe a target having dielectrically anisotropic microstructure as in the case of snow (Leinss et al., 2014).

$$\tilde{\gamma}_c = \frac{\langle S_{VV} S_{HH}^* \rangle}{\sqrt{\langle S_{VV} S_{VV}^* \rangle \langle S_{HH} S_{HH}^* \rangle}} = \gamma_c e^{j\phi_{CPD}}, \gamma_c \in [0, 1] \quad (2.2)$$

where,  $j$  is the imaginary unit.

### 2.2.2. Depolarisation Factor Estimation

130 In order to model this snow anisotropy, an ice particle needs to be associated with a specific shape. It has been observed that fresh snow and old snow exhibit horizontally aligned (oblate) and vertically aligned (prolate) spheroidal structures respectively (Leinss et al., 2014). Moreover, a shape parameter, known as the depolarisation factor, also has to be considered in this context  
 135 (Leinss et al., 2014; Sihvola, 1999). In principle, a single spheroidal particle is characterised by three dipoles corresponding to the three orthogonal axes ( $a_x$ ,  $a_y$ , and  $a_z$ ) represented using a 3D ( $x, y, z$ ) Cartesian coordinate system. This is depicted in Figure 2.2, where the prolate shaped ice grain is linked with the radar reference frame ( $h, k, v$ ) following the radar backscattering alignment (BSA)  
 140 convention,  $k$  being the propagation vector,  $h$  and  $v$  are the wave components of the horizontal and vertical polarisations respectively. Also,  $\theta$  is the mean incidence angle with respect to the surface normal (Leinss et al., 2014; Parrella et al., 2013).

Therefore, by fixing a particle shape, the three depolarisation factors,  $N_i$   
 145 ( $\forall i \in \{x, y, z\}$ ), can be obtained by solving the surface integral ( $s$  is the ellipsoidal surface) as shown in Eq. (2.3).

$$N_i = \frac{a_x a_y a_z}{2} \int_0^\infty \frac{ds}{(s + a_i^2) \sqrt{(s + a_x^2)(s + a_y^2)(s + a_z^2)}} \quad (2.3)$$

where,  $N_x + N_y + N_z = 1$ .

For a perfectly spherical shape, all three depolarisation factors are equal to 1/3. The two other special cases include disk (1, 0, 0) and needle (0, 1/2, 1/2).  
 150 In cases of prolate and oblate spheroids, the closed form expressions are already available as shown in Eq. (2.4) (Sihvola, 1999). Here, the shape is dependent on the axial ratio ( $a_x/a_z$ ) which is used for calculating the prolate eccentricity,  $e_1 = \sqrt{1 - (a_x/a_z)^2}$ , and oblate eccentricity,  $e_2 = \sqrt{(a_x/a_z)^2 - 1}$  respectively, i.e., for prolate,  $a_x/a_z < 1$ , whereas for oblate, it is the reverse. However, for  
 155 general ellipsoids having different axes, the above surface integration needs to be explicitly solved.



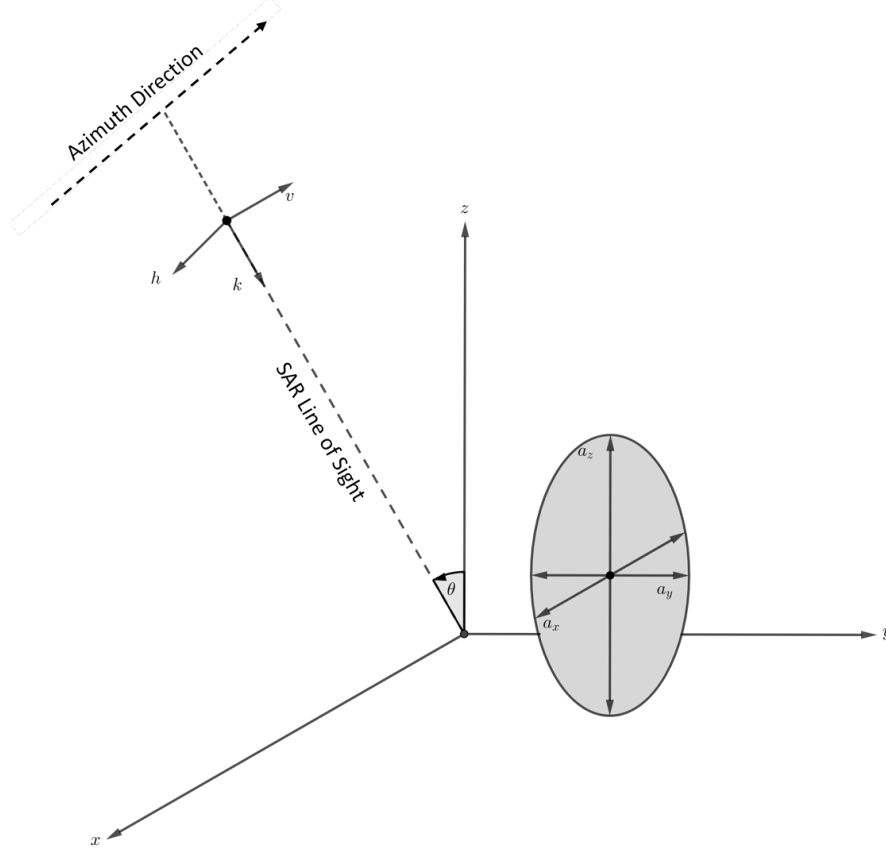


Figure 2.2: Orientation of a single prolate ice particle linked with the radar reference frame. Adapted from [Leinss et al. \(2014\)](#).

$$N_z = \begin{cases} \frac{1-e_1^2}{2e_1^3} \left( \ln \frac{1+e_1}{1-e_1} - 2e_1 \right) & , a_z > a_x = a_y \\ \frac{1+e_2^2}{e_2^3} \left( e_2 - \tan^{-1} e_2 \right) & , a_z < a_x = a_y \end{cases} \quad (2.4)$$

### 2.2.3. Snow Refractive Index Estimation

Evidently, the Maxwell-Garnett theory related to electromagnetic mixing models can be applied to a medium (here snow) consisting of both air and ice which are having relative permittivities (real part),  $\epsilon_{air}$  and  $\epsilon_{ice}$  respectively. Therefore, the effective permittivity of this mixed medium,  $\epsilon_{eff,i}$ , is anisotropic and given by Eq. (2.5) ([Leinss et al., 2014](#); [Sihvola, 1999](#)). Here, the particle

volume fraction ( $f_{vol}$ ) is dependent on the fresh snow density ( $\rho_f$ ) and ice density ( $\rho_{ice}$ ).

$$\epsilon_{eff,i} = \epsilon_{air} \left[ 1 + f_{vol} \frac{\epsilon_{ice} - \epsilon_{air}}{\epsilon_{air} + (1 - f_{vol}) N_i (\epsilon_{ice} - \epsilon_{air})} \right] \quad (2.5)$$

165 where,  $f_{vol} = \rho_f / \rho_{ice}$ ,  $\rho_{ice} = 0.917 \text{ g/cm}^3$ ,  $\epsilon_{air} = 1.00059$ ,  $\epsilon_{ice} = 3.179$ , and  $i \in \{x, y, z\}$ .

Furthermore, the refractive indices of this birefringent (or birefractive) medium,  $n_H$  and  $n_V$  corresponding to the HH and VV polarisations respectively, are dependent on this anisotropic effective permittivity (Leinss et al., 2014).  
 170 In addition, since the snow anisotropy is assumed to be oriented along the Earth's gravitational field,  $n_H$  remains constant whereas  $n_V$  is dependent on the incidence angle  $\theta$  as given by Eq. (2.6a) and Eq. (2.6b) respectively (Leinss et al., 2016). Also, the imaginary part of the effective permittivity is negligible in the case of dry snow (fresh snow is also dry), and therefore, it is not used in  
 175 the model developed by Leinss et al. (2014).

$$n_H^2 = \epsilon_{eff,x} \quad (2.6a)$$

$$n_V^2 = \epsilon_{eff,y} \cos^2 \theta + \epsilon_{eff,z} \sin^2 \theta \quad (2.6b)$$

where,  $\epsilon_{eff,x}$ ,  $\epsilon_{eff,y}$ , and  $\epsilon_{eff,z}$  represent the effective permittivities of fresh snow in  $x$ ,  $y$ , and  $z$  directions of a 3D Cartesian co-ordinate system (Leinss et al., 2014).

#### 2.2.4. FSD and FSWE Computation

180 Once all these aforementioned parameters are calculated, the CPD based inversion model given by Eq. (2.7) is applied to estimate the depth of fresh snow, denoted by  $\Delta Z_f$  (Majumdar et al., 2019; Leinss et al., 2014, 2016). In this equation, -1 is introduced as per the BSA convention which is followed for all radar systems. Here,  $\lambda_0$  is the radar wavelength and  $\Delta \zeta$  is the relative path  
 185 length difference which is dependent on  $\epsilon_{eff,i}$ ,  $\theta$ , and  $\rho_f$  (Leinss et al., 2016). Moreover, the horizontally aligned microstructure of fresh snow reduces the

propagation speed for the HH channel and hence, in this case,  $n_H > n_V$  always holds. However, for recrystallised snow having vertically aligned structures, the reverse condition is true (Leinss et al., 2016). Also, the LIA ( $\theta_l$ ) is used instead  
 190 of the mean incidence angle ( $\theta$ ) to consider the effect of the terrain slope.

$$\Delta Z_f = \left\langle (-1) \frac{\lambda_0 \phi_{CPD}}{4\pi \Delta \zeta} \right\rangle \quad (2.7)$$

where,  $\Delta \zeta = \sqrt{n_V^2 - \sin^2 \theta_l} - \sqrt{n_H^2 - \sin^2 \theta_l}$ ,  $\phi_{CPD} > 0$ , and  $n_H > n_V$ .

Here, the depolarisation factors are calculated by setting the axial ratio,  $a_x/a_z = 1.5$  in Eq. (2.4) and choosing the snow particle shape as an oblate (Majumdar et al., 2019). After this, the anisotropic effective permittivities  
 195 are computed using Eq. (2.5). Finally, the FSD is obtained from Eq. (2.7) wherein an ensemble averaging filter of size  $65 \times 65$  is applied. The FSWE is obtained by multiplying the FSD with the fresh snow density (i.e, FSWE =  $\rho_f \Delta Z_f$ ). Also, the fresh snow density ( $\rho_f = 0.07 \text{ g/cm}^3$ ) which is manually measured at Dhundi, is kept constant for the entire study area along with the  
 200 copolar coherence threshold,  $\tau_c = 0$  ( $\tau_c \in [0, 1]$ ), i.e., no thresholding has been applied on  $\gamma_c$  computed using Eq. (2.2), but the provision for it is built-in to the implementation. Moreover, as per the TSX/TDX metadata, the radar wavelength,  $\lambda_0 \approx 3.11 \text{ cm}$ . In this context, the adopted workflow is depicted in Figure 2.3.

### 205 2.3. Pol-InSAR based Standing Snow Depth Estimation

Standing or old snow refers to the deposited snow on the ground which has accumulated over time (Reynolds, 1983). Typically, old snow due to the presence of impurity and temperature-gradient induced recrystallisation process consists of snow particles larger than the microwave wavelength and results in volume  
 210 scattering (Leinss et al., 2016; Riche et al., 2013). This volume decorrelation can be quantitatively analysed with the help of the Pol-InSAR technique (Cloude, 2010) to obtain the volumetric SSD ( $\Delta Z_s$ ).

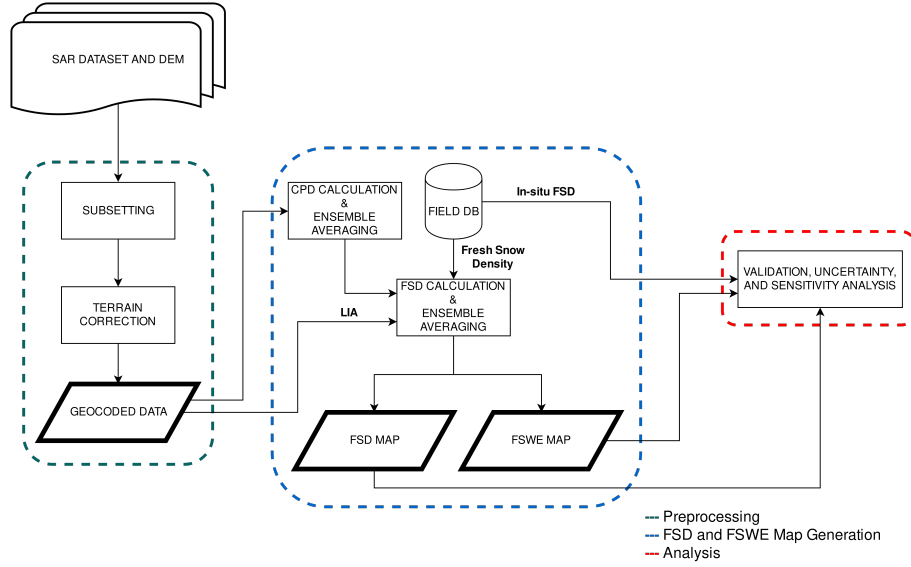


Figure 2.3: FSD and FSWE estimation workflow using PolSAR CPD. This workflow represents a detailed overview of the FSD and FSWE processing block in Figure 2.1.

### 2.3.1. Single-baseline Pol-InSAR Specifics

The single baseline Pol-InSAR algorithm works on the basis of the complex coherence,  $\tilde{\gamma}(\vec{w}_1, \vec{w}_2)$ , defined in Eq. (2.8a) where  $I_i(\vec{w}_1, \vec{w}_2)$  denotes the  $i^{\text{th}}$  pixel coordinate value of the wrapped Pol-InSAR interferogram,  $I(\vec{w}_1, \vec{w}_2)$  obtained in Eq. (2.8b). This interferogram is calculated from Eq. (2.8c) and Eq. (2.8d) where the coregistered master ( $s_1$ ) and slave ( $s_2$ ) images are acquired at a given polarisation vector,  $(\vec{w})$  respectively. Here, the weight vectors,  $\vec{w}_1$  and  $\vec{w}_2$  are selected by the user based on the scattering mechanisms at ends 1 and 2 of the interferometric baseline. If  $\vec{w}_1 = \vec{w}_2$ ,  $\tilde{\gamma}(\vec{w}_1, \vec{w}_2)$  can be alternatively specified as  $\tilde{\gamma}(\vec{w}_1)$  (Cloude, 2005, 2010). Moreover,  $L$  is the total number of pixels averaged in the range and azimuth directions which can be replaced by the ensemble averaging operation following the statistical ergodicity assumption (Hanssen, 2001; Hoen & Zebker, 2000; Kugler et al., 2015; Kumar et al., 2017; Papathanassiou & Cloude, 2001). Additionally,  $\phi_{flat}^w \in [0, 2\pi)$  is the wrapped flat-earth phase obtained from the estimated absolute flat-earth phase,  $\phi_{flat}$  and

has to be removed from  $I(\vec{w}_1, \vec{w}_2)$  as shown in Eq. (2.8b). Also, the calculation of the generalised weight vector,  $\vec{w}$  is given by Eq. (2.8e).

$$\tilde{\gamma}(\vec{w}_1, \vec{w}_2) = \frac{\sum_{i=1}^L I_i(\vec{w}_1, \vec{w}_2)}{\sqrt{\sum_{i=1}^L |s_{1i}(\vec{w}_1)|^2 \sum_{i=1}^L |s_{2i}(\vec{w}_2)|^2}}, |\tilde{\gamma}(\vec{w}_1, \vec{w}_2)| \in [0, 1] \quad (2.8a)$$

$$I(\vec{w}_1, \vec{w}_2) = s_1(\vec{w}_2) s_2^*(\vec{w}_2) e^{-j\phi_{flat}} \quad (2.8b)$$

$$s_1 = w_1^1 \frac{s_{hh}^1 + s_{vv}^1}{\sqrt{2}} + w_1^2 \frac{s_{hh}^1 - s_{vv}^1}{\sqrt{2}} + w_1^3 \sqrt{2} s_{hv}^1 \quad (2.8c)$$

$$s_2 = w_2^1 \frac{s_{hh}^2 + s_{vv}^2}{\sqrt{2}} + w_2^2 \frac{s_{hh}^2 - s_{vv}^2}{\sqrt{2}} + w_2^3 \sqrt{2} s_{hv}^2 \quad (2.8d)$$

$$\vec{w} = \begin{bmatrix} w^1 & w^2 & w^3 \end{bmatrix}^T = \begin{bmatrix} \cos \alpha & \sin \alpha \cos \beta e^{j\delta} & \sin \alpha \sin \beta e^{j\mu} \end{bmatrix}^T \quad (2.8e)$$

230 where,  $s_{pp}^1$  and  $s_{pp}^2$  correspond to the master (1) and slave (2) images respectively,  $pp \in \{hh, hv, vv\}$ , and  $*$  denotes the complex conjugate operator.

In this case, the parameters, scattering alpha angle ( $\alpha$ ), target orientation angle ( $\beta$ ), phase terms ( $\delta$  and  $\mu$ ), are chosen according to the selected polarisation given by Table 2.1. Here, LL, LR and RR correspond to the  
 235 left circular, left-right circular and right circular polarisations (Cloude, 2010). However, it is possible to optimise these parameters specific to the data, the details of which are provided by Cloude (2010).

Table 2.1: Pol-InSAR scattering mechanisms (Cloude, 2005).

| Polarisation Selection | $\alpha(^{\circ})$ | $\beta(^{\circ})$ | $\delta(^{\circ})$ | $\mu(^{\circ})$ |
|------------------------|--------------------|-------------------|--------------------|-----------------|
| HH                     | 45                 | 0                 | 0                  | 0               |
| HV                     | 90                 | 90                | 0                  | 0               |
| VV                     | 45                 | 180               | 0                  | 0               |
| HH+VV                  | 0                  | 0                 | 0                  | 0               |
| HH-VV                  | 90                 | 0                 | 0                  | 0               |
| LL                     | 90                 | 45                | 0                  | 90              |
| LR                     | 0                  | 0                 | 0                  | 0               |
| RR                     | 90                 | 45                | 0                  | -90             |

### 2.3.2. Height Inversion Algorithm Details

In this study, the modified (also improved) hybrid DEM differencing and  
 240 coherence amplitude based Pol-InSAR volumetric height inversion model as  
 given by Eq. (2.9a) is used for the SSD estimation. Firstly, the volume scattering  
 dominant channels, HV and VH, are averaged to fully utilise the quad-pol data  
 (Cloude, 2005). Next, the Pol-InSAR interferogram,  $I(\vec{w}_v)$  has been computed  
 using Eq. (2.8b) wherein, the weight vector,  $\vec{w}_v$  is obtained from Table 2.1  
 245 for the HV polarisation. Thereafter, the complex volume coherence,  $\tilde{\gamma}(\vec{w}_v)$ ,  
 is calculated from Eq. (2.8a) with  $L = 3$ . Similarly, the complex surface or  
 ground coherence,  $\tilde{\gamma}(\vec{w}_s)$ , is computed by choosing  $\vec{w}_s$  as the HH-VV weight  
 vector (Table 2.1).

Moreover, the actual vertical wavenumber,  $k_z$ , when varied with the LIA, is  
 250 in the order of 0.1 rad/m with the ambiguity height,  $h_{2\pi} = 2\pi/k_z \approx 63.18$  m,  
 $\lambda_0 \approx 3.11$  cm and  $m = 1$  (single-pass acquisition). Since the maximum height of  
 the distributed volume scatterer (in this case, standing snow),  $\Delta Z_{s,max}$ , should  
 be similar to  $h_{2\pi}$  (Kugler et al., 2015; Hajnsek et al., 2009; Kumar et al., 2017),  
 $k_z$  has to be rescaled to an optimum range for effectively estimating the SSD.  
 255 Hence, the modified vertical wavenumber,  $k'_z$ , is given by Eq. (2.9b) where  $\eta'$   
 is a free scaling parameter which has to be set according to the known  $\Delta Z_{s,max}$   
 in the study area. Here,  $h'_{2\pi}$  is the scaled height of ambiguity which like that  
 of  $h_{2\pi}$  determines the height changes in modulo  $2\pi$  (Hanssen, 2001). Also,  $\mathbb{R}^+_{>0}$   
 denotes the set of all positive real numbers in the interval  $(0, \infty)$ . In this work,  
 260 due to the limited ground-truth data availability and the subsequent ensemble  
 averaging operation (window size of  $21 \times 21$ ) on  $k'_z$ ,  $\Delta Z_{s,max} = 12$  m has been  
 assumed for which  $\eta' = 5$  is used.

Apart from this, the function  $\arg$  is defined in the interval  $[0, 2\pi)$  and the  
 parameter  $m$  is set to 1 for bistatic acquisition and 2 in the monostatic case.  
 265 Also in Eq. (2.9b),  $\Delta\theta$  is the change in the incidence angle occurring due to  
 the spatial baseline,  $\theta_l$  is the LIA, and  $\lambda_0$  is the radar wavelength as before in

section 2.2 (Cloude, 2010; Kugler et al., 2015).

$$\Delta Z_s = \frac{\arg\left(\tilde{\gamma}(\vec{w}_v) e^{-j\phi_{topo}^w}\right)}{k'_z} + \eta \frac{\text{sinc}_\pi^{-1}(\gamma(\vec{w}_v))}{k'_z}, \eta \in [0, 1] \quad (2.9a)$$

where,

$$k'_z = \left\langle \eta' \frac{m\Delta\theta}{\lambda_0 \sin\theta_t} \right\rangle, \eta' \in \mathbb{R}_{>0}^+ \mid \Delta Z_{s,max} \approx h'_{2\pi} = 2\pi/k'_z \quad (2.9b)$$

Subsequently, the volume and surface coherences are then used to estimate  
 270 the wrapped ground phase,  $\phi_{topo}^w \in [0, 2\pi)$ , from Eq. (2.10). Additionally, a  
 median ensemble filter of  $21 \times 21$  is applied on the obtained  $\phi_{topo}^w$  following the  
 processing steps provided by Cloude (2005).

$$\phi_{topo}^w = \arg\left(\tilde{\gamma}(\vec{w}_v) - \tilde{\gamma}(\vec{w}_s)(1 - L_{\vec{w}_s})\right) \quad (2.10)$$

where,

$$L_{\vec{w}_s} = \frac{-B - \sqrt{B^2 - 4AC}}{2A}, L_{\vec{w}_s} \in [0, 1]$$

$$A = |\tilde{\gamma}(\vec{w}_v)|^2 - 1$$

$$B = 2\Re(\tilde{\gamma}(\vec{w}_v) - \tilde{\gamma}(\vec{w}_s)\tilde{\gamma}^*(\vec{w}_v))$$

$$C = |\tilde{\gamma}(\vec{w}_v) - \tilde{\gamma}(\vec{w}_s)|^2$$

Eventually, the SSD ( $\Delta Z_s$ ) and SSWE ( $= \rho_s \Delta Z_s$ ) are estimated wherein  
 the standing snow density ( $\rho_s = 0.315 \text{ g/cm}^3$ ) measured by the Dhundi SPA at  
 275 06:22 hrs IST on January 8, 2016, has been used. Here,  $\eta = 0.65$ , the volume  
 coherence threshold,  $\tau_v = 0.6$  (pixels having  $\tau_v < 0.6$  are neglected  $\forall \tau_v \in [0,$   
 $1]$ ), and the SSD values are averaged based on a  $57 \times 57$  ensemble filter window.  
 The entire Pol-InSAR workflow is summarised in Figure 2.4 which shows the  
 main processing blocks.

280 However, in order to compute the inverse  $\text{sinc}_\pi$  (normalised sinc) function  
 in Eq. (2.9a), the Cloude (2010) approximation ( $\text{sinc}_C^{-1}$ ) in Eq. (2.11a) is  
 replaced by Eq. (2.11b) where the secant method (Cheney & Kincaid, 2012)  
 has been applied to find  $\alpha_r \in \mathbb{R}$  (rad), the desired root or inverse. Moreover, to

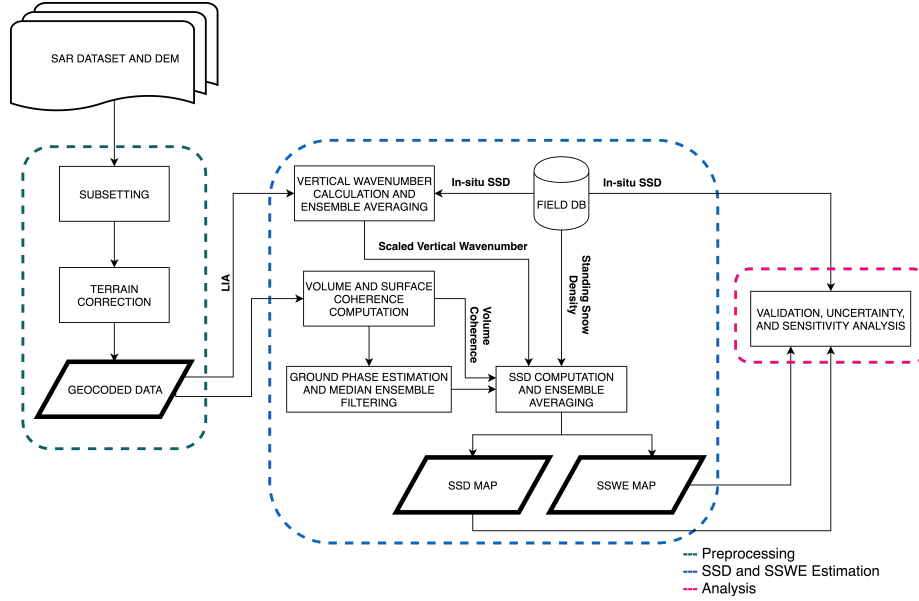


Figure 2.4: SSD and SSWE estimation workflow using Pol-InSAR depicting a detailed overview of the SSD and SSWE processing block in Figure 2.1.

make the Cloude (2010) approximation compliant with the scientific computing  
 285 libraries such as SciPy (Jones et al., 2001) which use the  $\text{sinc}_\pi$  function, the  
 normalised variant of Eq. (2.11a) given by Eq. (2.11c) is incorporated where  
 $\text{sinc}_{\pi_C}^{-1}$  denotes the inverse of the  $\text{sinc}_\pi$  function computed using the Cloude  
 (2010) approach. Similarly,  $\text{sinc}_{\pi_S}^{-1}$  represents the inverse of the  $\text{sinc}_\pi$  function  
 290 obtained by applying the secant method (Cheney & Kincaid, 2012; Jones et al.,  
 2001). This root finding technique has been deployed as it is more accurate  
 than the given approximation in Eq. (2.11c), the analysis of which is described  
 in section 4. Still, in the Python implementation, this approximation is used as  
 an initial guess to the secant method for faster convergence. It is also used as a  
 fallback option if the secant method is unable to converge within 50 iterations



295 or the default convergence threshold of 1.4E-8 (Jones et al., 2001).

$$\text{sinc}_C^{-1}(\gamma(\vec{w}_v)) = \pi - 2 \sin^{-1}\left(\gamma(\vec{w}_v)^{0.8}\right) \quad (2.11a)$$

$$\text{sinc}_\pi \alpha_r - \gamma(\vec{w}_v) = 0 \quad (2.11b)$$

$$\text{sinc}_{\pi_C}^{-1}(\gamma(\vec{w}_v)) = \frac{\text{sinc}_C^{-1}(\gamma(\vec{w}_v))}{\pi} \quad (2.11c)$$

## 2.4. Validation, Uncertainty Assessment, and Sensitivity Analysis

### 2.4.1. Validation Process

One of the significant challenges in this work is the limited ground-truth data availability. Since, in-situ data from only two ground stations are available, the conventional way of accuracy assessment through regression plots (Kugler  
300 et al., 2015; Leinss et al., 2014; Kumar et al., 2017) is infeasible in this context. Moreover, the Kothi AWS area falls in the layover region for the descending pass acquisitions and hence, only the Dhundi region which is free from layover, shadow and foreshortening effects, is used for validation. In this case, a neighbourhood window of size 3×3 ( $\approx 81 \text{ m}^2$  ground area) surrounding the  
305 Dhundi SPA is selected for validating the SD and SWE estimates by considering only the statistical mean and standard deviation.

### 2.4.2. Uncertainty Assessment

Due to the complex terrain characteristics there exist significant uncertainty  
310 sources which could potentially lead to the overall degradation of the output accuracy. Having the quad-pol data in winter time (January 8, 2016) and dual-pol data in summer time, we are able to use dual-pol entropy ( $H \in [0, 1]$ ) and the scattering alpha angle ( $\alpha \in [0^\circ, 90^\circ]$ ) or  $H/\alpha$  decomposition to comparatively understand the backscattering mechanisms in these two time intervals (Cloude,  
315 2010; Lee & Pottier, 2009; Singh et al., 2014). The 5×5 window size for the  $H/\alpha$  decomposition is used. This is carried out through the  $H/\alpha$  plane plot which demarcates eight feasible zones (Z9 being the unclassified pixels) based on the different scattering classes as shown in Figure 2.5. Note that, this diagram which

follows the SNAP style (ESA, 2018), uses slightly different labels as compared to the Lee & Pottier (2009)  $H/\alpha$  plane convention where the labels Z1, Z2, Z3 are denoted as Z7, Z8, Z9 and vice-versa respectively. However, the scattering mechanisms are exactly the same in both these conventions. Here, the blue curve acts as a boundary to the plane which essentially denotes the reliability of the classification in high entropy conditions (Brunner, 2009).

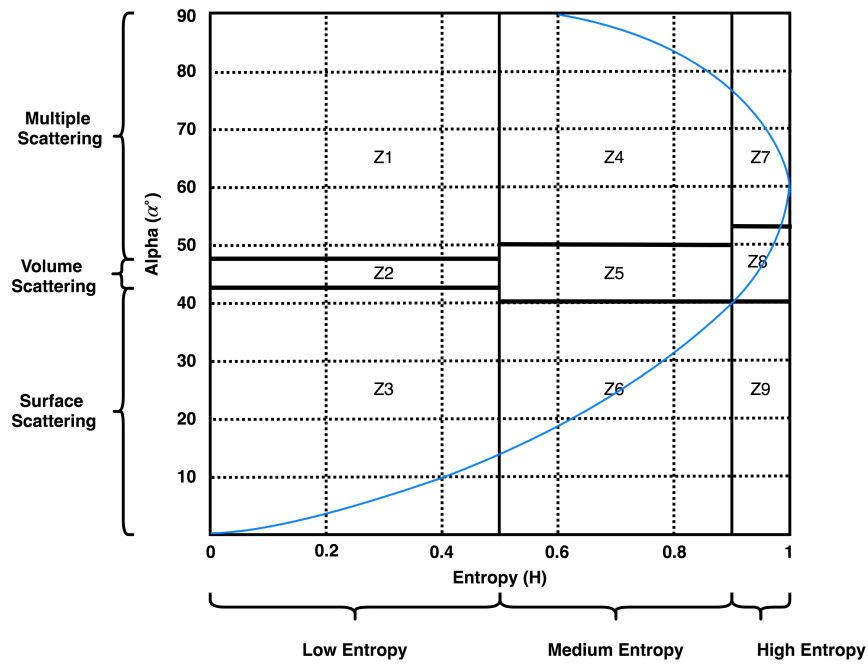


Figure 2.5:  $H/\alpha$  plane showing different scattering zones. Z1: Dihedral, Z2: Dipole, Z3: Bragg Surface, Z4: Double bounce, Z5: Anisotropic, Z6: Random surface, Z7: Complex structures, Z8: Random anisotropic, Z9: Non-feasible.

The dual-pol  $H/\alpha$  decomposition is further used by the unsupervised Wishart classifier (ten iterations) which classifies the SAR data based on these scattering mechanisms and a quantitative estimate of the number of pixels in each such class can be obtained (Cloude, 2010; Lee & Pottier, 2009). Therefore, by knowing the scattering properties, the terrain features present in the study area can be understood along with their changes during the snow season. In turn, these ground features which include rough surfaces, shrubs, boulders,

and human settlements reduce the copolar coherence amplitude ( $\gamma_c$ ) thereby leading to underestimated FSD results (Leinss et al., 2014, 2016). In addition, the decrease in the Pol-InSAR surface coherence amplitude, ( $\gamma(\vec{w}_v) = |\tilde{\gamma}(\vec{w}_v)|$ ) may result in overestimated volumetric height (Cloude, 2010; Hajnsek et al., 2009; Kugler et al., 2015), in this case, SSD. Thus, the uncertainty assessment by means of the identification of the backscattering mechanisms constitutes a key role in this work.

Apart from this, the forest cover map (obtained from WRD, IIRS) along with the layover and shadow regions computed using SAR simulation are used to mask out the noisy pixels which degrade the quality of the results. This is a standard approach used in the studies focusing on snow property estimation in forested or alpine terrains (Leinss et al., 2014, 2016; Singh et al., 2017; Thakur et al., 2012; Usami et al., 2016).

#### 2.4.3. Sensitivity Analysis

The variation of the SD and SWE values corresponding to the changes in the free parameters in the FSD and SSD inversion models (window size, coherence threshold, scaling factors) are observed by iteratively running the algorithms and computing the statistical mean and standard deviation using the neighbourhood window discussed earlier in section 2.4.1. This helps in deciding the window shape and sizes and also choosing the optimum values for the several free parameters. Moreover, the accuracy of the root finding algorithm discussed in section 2.3 is also checked for some possible coherence values.

In addition, the ground elevation measurements acquired during the field visit to Dhundi and Kothi were compared with the ALOS PALSAR DEM elevations ( $z$ ). The effect of the DEM errors on the LIA,  $\theta_l$ , is then checked for performing the sensitivity analysis (SA) using Eq. (2.12) which incorporates the slope angles in  $x$  ( $\omega_x$ ) and  $y$  ( $\omega_y$ ) directions (pixel co-ordinate system where  $z$  is the corresponding elevation value) derived from the DEM elevation values along with the radar incidence angle ( $\theta$ ) (Lee et al., 2000; Lee & Pottier, 2009). Here, the terms  $dz/dx$  and  $dz/dy$  refer to the rate of elevation ( $z$ ) change in

the  $x$  and  $y$  directions respectively.

$$\theta_l = \cos^{-1} \frac{\cos \omega_x \cos (\omega_y - \theta)}{\sqrt{\cos^2 \omega_y \sin^2 \omega_x + \cos^2 \omega_x}} \quad (2.12)$$

where,

$$\omega_x = \tan^{-1} \frac{dz}{dx}, \omega_y = \tan^{-1} \frac{dz}{dy}.$$

### 3. Study Area, Datasets, and Software

#### 3.1. Chosen Study Area

##### 3.1.1. Geographical Situation

The Beas river watershed near Manali, India is part of the north-western Himalayas. Naturally, steep slopes and dense forests are prominent in this region. The elevation typically varies from nearly 2500 m to more than 5000 m in some places as observed in the reference ALOS PALSAR DEM (Figure 3.1).

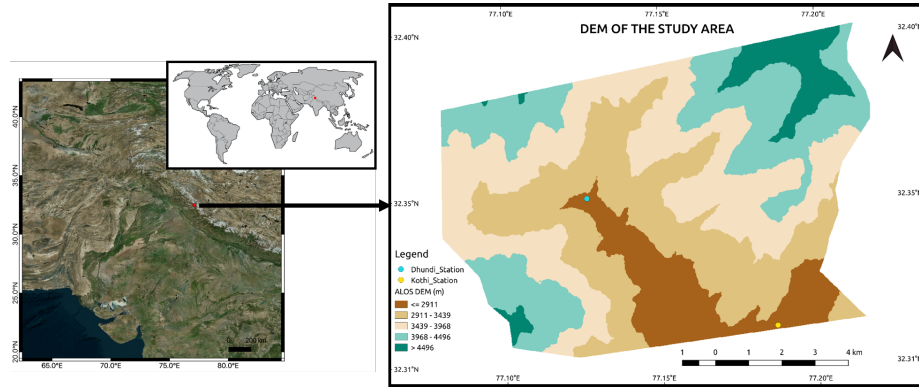


Figure 3.1: Overview map of the study area showing the ALOS PALSAR DEM. The original DEM of 12.5 m spatial resolution (generated in 2011) has been resampled to 3 m using bilinear interpolation (Wu et al., 2008) to match the high resolution SAR data. Moreover, the vertical resolution as per the product specification is 5 m.

In this work, a small region ( $\sim 96 \text{ km}^2$ ) of the Beas basin is chosen which starts a few kilometres uphill from Dhundi up to Kothi (shown in Figure 3.1). These areas receive substantial seasonal snowfall which begins in December and

lasts till late March. However, the cold, dry season usually commences from late September or early October. The coldest period is in January during which  
375 the temperatures reach a daily minimum of  $-15^{\circ}\text{C}$  on an average. The summers are mild to occasionally warm with June being the hottest month (mean and maximum temperatures of  $20^{\circ}\text{C}$  and  $30^{\circ}\text{C}$  respectively are common). Apart from this, significant rainfall occurs between late June and September (monsoon season) with August receiving the maximum precipitation ([Majumdar et al., 2019](#); [Thakur et al., 2012](#)).  
380

### *3.1.2. Field Visit*

Intensive fieldwork had been conducted from October 14-21, 2018 in the Dhundi and Kothi areas where several Differential Global Positioning System (DGPS) measurements were acquired using the Leica Viva GS 10 ([Leica Geosystems AG, 2012](#)) with adequate horizontal positional accuracies ( $\sim 7$  cm)  
385 ([Majumdar et al., 2019](#)). Due to the complex terrains, most of the DGPS readings had been obtained through the kinematic mode ([Luo et al., 2014](#)). However, in some of the convenient places such as the Dhundi base station and near the Kothi Automatic Weather Station (AWS), the static mode was used  
390 ([Leica Geosystems AG, 2012](#)). Eventually, elevation information from these DGPS points have been compared with the ALOS PALSAR DEM, the details of which are provided in section 4. Furthermore, the manual snow readings from 2014-2018 (snow depth, density, weather profile and other relevant data) which are maintained by the security personnel daily at Dhundi had been pagewise  
395 photographed using a smartphone camera. In order to properly understand and visualise the characteristics of the study area, selected field photographs and their brief description are shown from figures [3.2\(a\)](#)-[3.2\(f\)](#).

### *3.2. Datasets Used*

Overall twelve Coregistered Single look Slant range Complex (CoSSC)  
400 TerraSAR-X (TSX)/TanDEM-X (TDX) bistatic X-band SAR images acquired between December 2015 and August 2017 in stripmap (SM) mode are available



Figure 3.2: Dhundi field photographs showing the varying topographic features present in the surrounding area.

over this study area (Bals et al., 2012). In total, there are six Quad-pol data pairs, from which the descending orbital pass acquisition at 00:53 hrs Universal Time Coordinated (UTC), January 8, 2016, has been selected considering  
405 the occurrence of fresh snowfall before, during and after the satellite flyby. Moreover, the perpendicular baseline ( $B_{\perp}$ ) and ambiguity height ( $h_{2\pi}$ ) for this data are 96.34 m and 63.18 m respectively.

Additionally, the in-situ snow physical parameters data (standing and fresh snow depths, snow density) along with the relevant weather data had been

410 transferred to a PostgreSQL database (DB) ([PostgreSQL, 2019](#)) from the  
photographs of the manual recordings through spreadsheets. Apart from this,  
the high frequency data (two-minute interval measurements) obtained from the  
snowpack analyser (SPA) device (installed at Dhundi) had been downloaded and  
were added to the database as a separate table. Accordingly, the SSDs at 06:22  
415 hrs (00:52 hrs UTC) Indian Standard Time (IST) on January 7, 2016, and 06:22  
hrs January 8, 2016 morning were 36.2 cm and 54.9 cm respectively signifying  
a heavy fresh snowfall event of 18.7 cm within 24 hrs. The manual recordings  
also showed an FSD of 18 cm on January 8, 2016 morning though the exact  
measurement time is unspecified in the record book. Apart from this, a forest  
420 mask used in the earlier studies of this area ([Thakur et al., 2012, 2017](#)) has  
been obtained from the Water Resources Department (WRD), Indian Institute  
of Remote Sensing (IIRS).

The Sentinel Application Platform (SNAP) 6.0.5 ([ESA, 2018](#)) has been used  
for basic SAR processing. In addition, the FSD and SSD inversion models have  
425 been implemented using Python 3 wherein PyCharm Community Edition 2018.1  
([JetBrains, 2018](#)) was used as the coding environment. Moreover, the final snow  
depth maps have been prepared using QGIS 2.18 ([QGIS, 2016](#)). Furthermore,  
some of the computationally intensive tasks have been carried out using the  
High-Performance Computing (HPC) infrastructure installed at IIRS.

## 430 **4. Results and Discussion**

### *4.1. Scattering Mechanisms*

The winter (January 8, 2016) and summer-time (June 8, 2017) dual-pol  $H/\alpha$   
decomposition (Figure 4.3) and unsupervised Wishart classification (Figure 4.1)  
results combined with the derived class percentage statistics (Figure 4.2) show  
435 that, in the presence of snow, the high entropy anisotropic volume scattering  
(Z8) increases by 5.11% whereas the medium entropy volume scattering (Z5)  
decreases by 7.01% for the entire study area. This reduction in the Z5  
volume scattering could be attributed to the partially snow covered forests and

shrubs which exhibit higher volume scattering at X-band during the snow-free  
 440 season (Figure 3.2(e)). The corresponding dual-pol Wishart classified maps  
 are displayed along with the zoomed views in Figure 4.1(a) and Figure 4.1(b)  
 respectively.

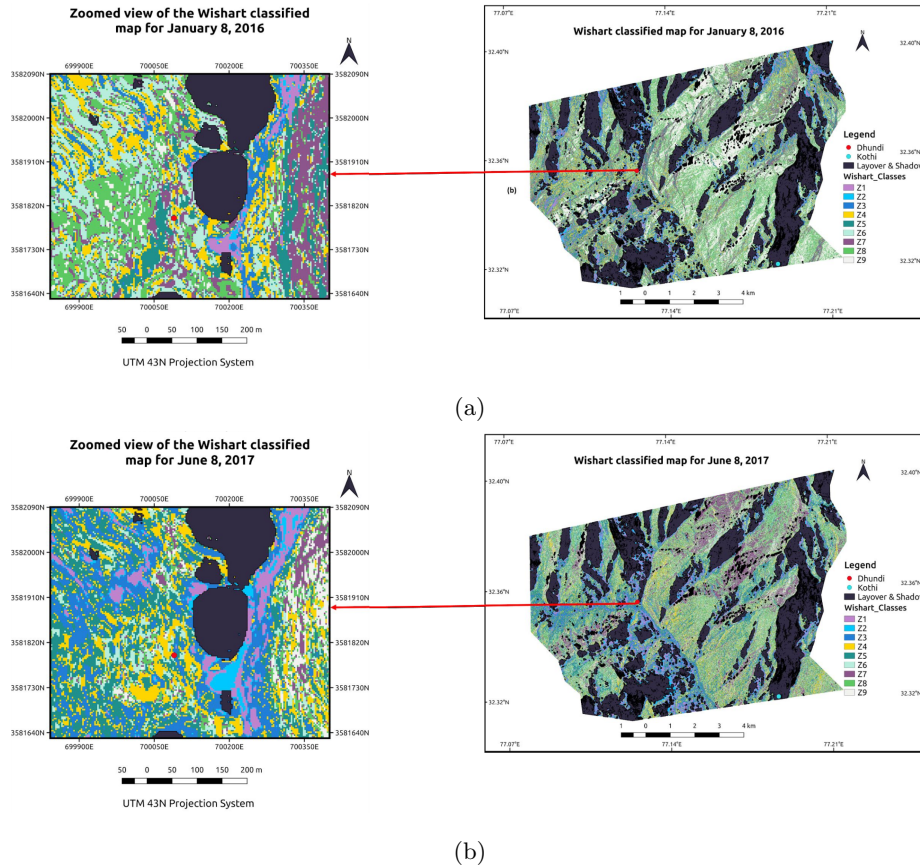


Figure 4.1: Zoomed views over Dhundi of the Wishart classified maps for the (a) January 8, 2016, and (b) June 8, 2017 data. Here, only the layover and shadow mask has been applied. Also, the Kothi area is excluded from the analysis since it lies in the layover region.

Moreover, the Bragg surface scattering (Z3) is slightly higher in summer  
 (10.88%) as compared to the winter (10.38%). One plausible reason for this  
 445 is the 20 mm rainfall which occurred on June 7, 2017, evening (data retrieved from  
 the Dhundi record book). Also, the occurrence of fresh snowfall in areas which



did not have prior standing or old snow could result in surface scattering from the ground (Leinss et al., 2014). Apart from this, the asbestos gable roofs used in the human settlements (Figure 3.2(b) and Figure 3.2(d)) are strong single-bounce surface scatterers (Brunner, 2009). However, with snow accumulation on these materials, the surface scattering could be reduced. Another prominent feature noticeable in Figure 4.1(b) is the high amount of surface scattering from the river bed (Figure 3.2(c)) during the summer season. This is caused by both the boulders and the increasing flow of snow-melt water in the river (Figure 3.2(c)).

Furthermore, the human settlements result in double-bounce scattering (Z4) (Brunner, 2009), which in the winter-time scenario reduces by 0.34%. Also, the random surface scattering (Z6) increases by 0.66% which could be caused by the presence of small snow patches on the ground. Other than this, there is a strong decrease in the low entropy multiple (dihedral) scattering from 8.23% to 5.17% in the snow-covered season which could be caused by the added snow layer on the buildings and also boulders.

Another interesting aspect in this context is the increase (from 9.93% to 19.8%) in the number of unclassified or non-feasible pixels (Z9) for the winter-time image (Figure 4.2) which is also depicted through the  $H/\alpha$  plane plots in Figure 4.3(a) and Figure 4.3(b). This is primarily resulting from the added terrain complexity owing to the snow accumulation. In order to resolve this issue, the quad-pol entropy ( $H$ ), anisotropy ( $A \in [0, 1]$ ), alpha ( $\alpha$ ),  $H/A/\alpha$  decomposition has been applied on the January 8, 2016 data. The corresponding  $H/\alpha$  plane plot in Figure 4.3(c) shows that the quad-pol approach is able to fully classify the winter-time image. However, since the summer-time image is having only HH and VV channels, the dual-pol method has been used to properly compare the respective scattering mechanisms (Majumdar et al., 2019).

Thus, from this discussion, it is clearly observed that the presence of snow causes a substantial change of the scattering patterns in the study area resulting in significant uncertainty sources. In turn, the optimisation of the model parameters along with the sensitivity analysis of the FSD and SSD values depend

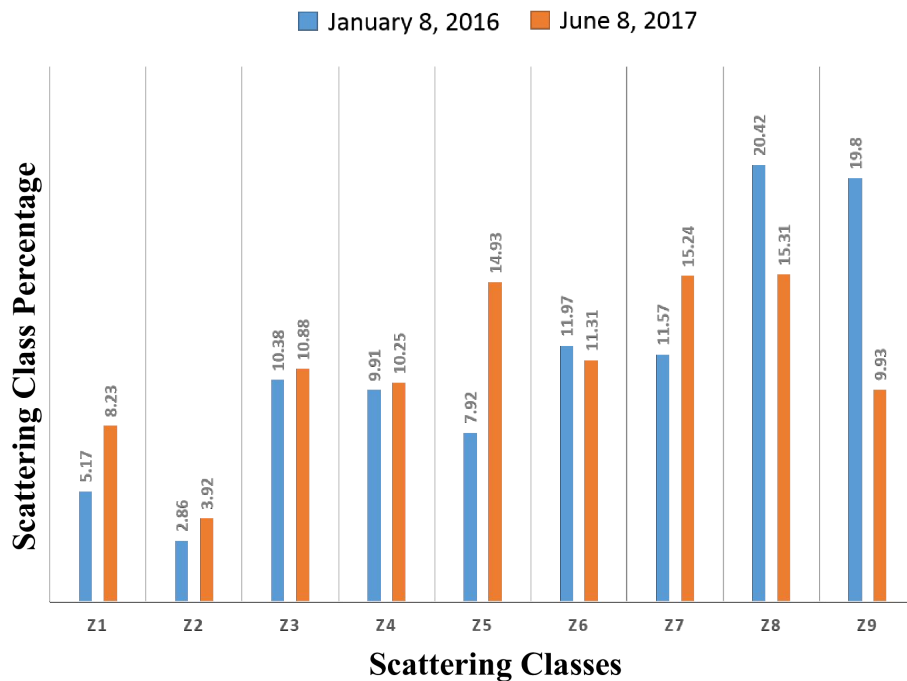


Figure 4.2: Scattering class percentages (rounded to 2 decimal places) from the unsupervised Wishart classification. The different zone labels are described in Figure 2.5.

on these scattering types. As an example, if there is low surface scattering then the FSD inversion model leads to underestimated values (Leinss et al., 2014) whereas for low volume scattering, the SSD results are generally underestimated (Cloude, 2005; Hajnsek et al., 2009; Kugler et al., 2015). Therefore, the uncertainty assessment by means of the scattering mechanism classification is one of the key aspects of this research.

#### 4.2. Sensitivity Analysis Results

In order to perform the sensitivity analysis, only the Dhundi area is chosen as Kothi is lying in the layover zone for this acquisition (January 8, 2016).

##### 4.2.1. FSD Parameters

The FSD inversion model discussed in section 2.2 applies the ensemble averaging operation twice—once on the computed CPD and then subsequently

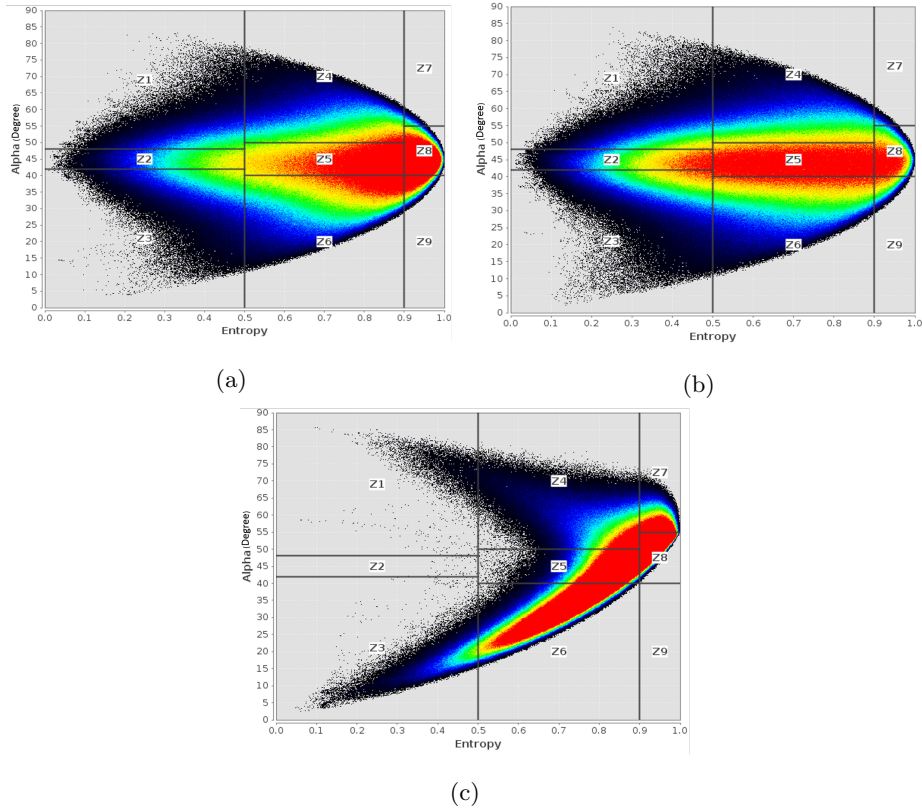


Figure 4.3: Dual-pol  $H/\alpha$  plane plots for the (a) January 8, 2016, and (b) June 8, 2017 data, (c) Quad-pol  $H/\alpha$  plane plot for the January 8, 2016 data. The colours red, green, blue, and black indicate the point density with red being the highest, and black as the lowest. These plots have been made using SNAP (ESA, 2018).

490 on the output FSD values. As a result, the selection of an optimal window size  
in both these cases is critical in obtaining reliable estimates. At first, the mean  
( $\mu_{\gamma_c}$ ) and standard deviation ( $\sigma_{\gamma_c}$ ) of the copolar coherence amplitude ( $\gamma_c$ ) are  
checked over the Dhundi area based on a  $3 \times 3$  neighbourhood window (same as  
the validation window in section 2.4.1). The ensemble window for which the  
495 maximum  $\mu_{\gamma_c}$  occurs is subsequently used for estimating the FSD following the  
methodology described in section 2.2. This selection procedure concerning the  
maximisation of  $\mu_{\gamma_c}$  is depicted in Figure 4.4 wherein the ensemble window of  
size  $3 \times 3$  is found to be suitable even though  $\sigma_{\gamma_c} \approx 0.06$  of this window is slightly

higher than that ( $\sigma_{\gamma_c} \approx 0.02$ ) of the  $5 \times 5$  window.

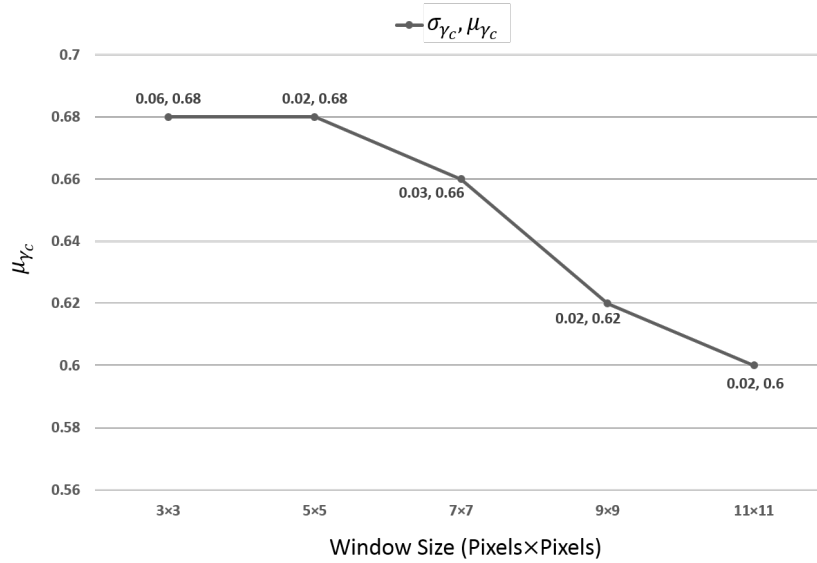


Figure 4.4: Effect of the window size on the mean and standard deviation of the copolar coherence amplitude. All the values are rounded to 2 decimal places. Here, only odd window sizes are considered because these have been previously used in prior studies (Leinss et al., 2018, 2014; Kumar & Venkataraman, 2011).

500 Next, the sensitivity of the FSD values with respect to the ensemble window size is taken into account. This is shown in Figure 4.5 where the analysis starts from the window size  $3 \times 3$  and continues till  $99 \times 99$  with an increment of two pixels in each direction (Figures 4.5(a) and 4.5(b)). In this context, smaller window sizes ( $< 45 \times 45$ ) are not considered following the work of Leinss  
505 et al. (2014) where a  $45 \times 35$  window size has been chosen. Similarly, higher window sizes ( $> 65 \times 65$ ) are not used because of the varying topography in the study area. Another reason is that, since the Dhundi region exhibits moderate undulating terrains, so from the validation perspective, window sizes which cover ground areas of more than  $0.4 \text{ km}^2$  are excluded from the analysis. Hence, the  
510 transect as shown in Figure 4.5(c) is used for deciding the FSD ensemble window size.

In this regard, the SPA measured FSD ground-truth data at 06:22 hrs

January 8, 2016 (IST) was 18.7 cm, and that of the manual record book was 18 cm (section 3.2). Assuming the SPA sensor bias to be 5 cm for the SD, the  
515 FSD ground observation of 18 cm is taken as the true value. Accordingly, it is observed from Figure 4.5(c) that the 65×65 window leads to the most accurate (94.83%) mean FSD ( $\mu_f \approx 18.93$  cm) with a low FSD standard deviation ( $\sigma_f \approx 0.1$  cm). The corresponding mean FSWE ( $\mu_{fs} \approx 13.25$  mm) and FSWE standard deviation ( $\sigma_{fs} \approx 0.07$  mm) are also in concordance (94.84% accuracy)  
520 with the ground-truth FSWE of 12.6 mm. However, it should be noted that the axial ratio for the fresh snow particle,  $a_x/a_z = 1.5$  is kept as an invariant throughout the entire FSD workflow (Figure 2.3) and its SA has not been carried out.

Here, the FSD and  $\gamma_c$  values are significantly influenced by the mixed  
525 scattering mechanisms exhibited by the ground features (Figure 4.1(a)) which are being considered for the averaging operation. Moreover, the underlying assumption of a smooth surface in the FSD inversion model does not hold for such rough terrains and consequently,  $\gamma_c$  is reduced (Leinss et al., 2014). Therefore, the FSD SA concludes that even though a sufficiently reliable FSD  
530 estimate has been achieved in the Dhundi area, the window sizes need to be adequately adjusted for different multi-temporal SAR images acquired over the same region thereby leading to a more robust parameter optimisation process.

#### 4.2.2. SSD Parameters

The SSD inversion model as described from the implementation or  
535 methodological perspective in section 2.3 incorporates several user-defined free parameters. Thus, it is necessary to conduct an appropriate SA for the hybrid Pol-InSAR based volumetric height (SSD) retrieval algorithm. Accordingly, the various model parameters and their optimisation are discussed below.

#### *Volume and Surface Coherence Ensemble Window*

540 The ensemble windows corresponding to the number of looks (L) in Eq. (12) must be suitably chosen so as to maximise both the volume coherence

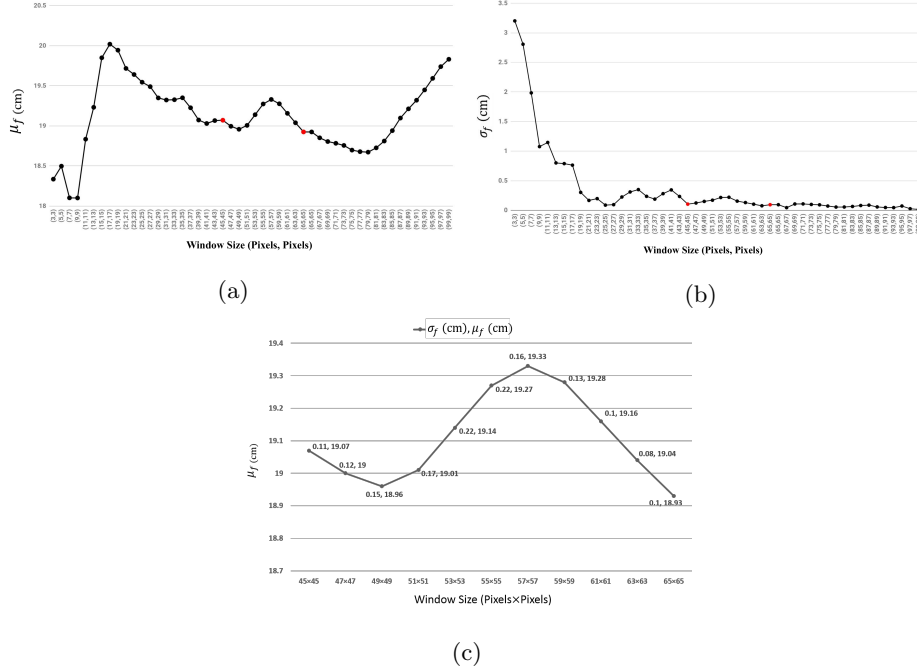


Figure 4.5: Effect of the window size on the (a) mean and (b) standard deviation of the FSD estimates. Here, the transect between the two red points ( $45 \times 45$  and  $65 \times 65$ ) are collectively shown in (c) wherein all the values are rounded to 2 decimal places.

amplitude,  $\gamma(\vec{w}_v)$ , and the surface coherence amplitude,  $\gamma(\vec{w}_s)$ . As a result, the SA for these window sizes is an important aspect of this work.

The effects of  $L$  on the mean volume coherence amplitude,  $\mu_{\gamma(\vec{w}_v)}$  and the  
545 mean surface coherence amplitude,  $\mu_{\gamma(\vec{w}_s)}$  which are measured by applying the same  $3 \times 3$  neighbourhood window over Dhundi (section 2.3) along with the respective standard deviations,  $\sigma_{\gamma(\vec{w}_v)}$  and  $\sigma_{\gamma(\vec{w}_s)}$ , are displayed in Figure 4.6.

It can be seen that for the executed test cases, with increasing  $L$ , there is a  
550 general decreasing trend for both these coherences. So, for the SSD estimation,  $L = 3$  is chosen even though Cloude (2005) suggests the usage of higher values of  $L$ . This is because,  $\sigma_{\gamma(\vec{w}_v)} \approx 0.1$  and  $\sigma_{\gamma(\vec{w}_s)} \approx 0.18$  are sufficiently small with adequately high  $\mu_{\gamma(\vec{w}_v)} \approx 0.67$  and  $\mu_{\gamma(\vec{w}_s)} \approx 0.68$ . Also, since there is only one validation point for the entire study area,  $L = 3$  is justifiable.

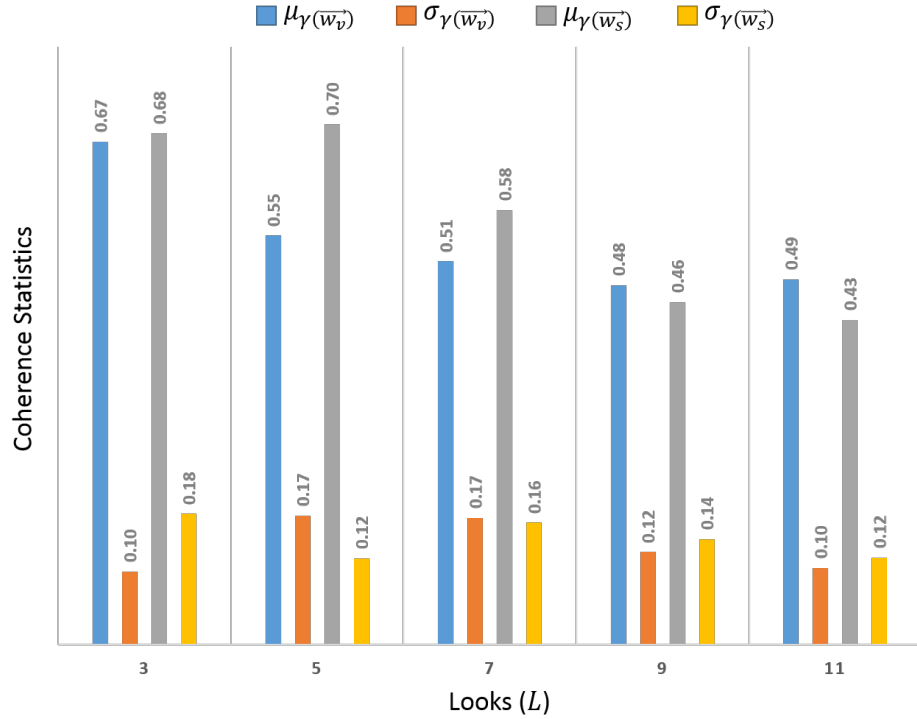


Figure 4.6: Effect of the number of looks ( $L$ ) on the volume and surface coherence. All the values are rounded to 2 decimal places.

However, there exist several free parameters in this Pol-InSAR based SSD inversion model (section 2.3) and hence, the volume and surface coherence ensemble windows need to be kept constant ( $L = 3$ ) for the subsequent SA of the other parameters.

### Scaling Parameters

It has been previously discussed in section 2.3 that there are two scaling parameters involved in the SSD estimation process. These are the vertical wavenumber scaling parameter ( $\eta' \in \mathbb{R}_{>0}^+$ ) and the scaling factor ( $\eta \in [0, 1]$ ) of the hybrid DEM differencing approach developed by Cloude (2010). Here, the SA of only  $\eta$  is carried out and  $\eta' = 5$  is kept constant throughout the entire workflow. Also, the volume coherence threshold,  $\tau_v = 0.6$ ,  $L = 3$ , ground phase median ensemble filter window ( $21 \times 21$ ), vertical wavenumber ensemble

average window ( $21 \times 21$ ), and the SSD ensemble average window of size  $57 \times 57$  are unchanged during this SA.

The monotonically increasing SSD with respect to increasing  $\eta$  are displayed in Figure 4.7. For  $\eta = 0$ , the standard DEM differencing technique (Cloude, 2005) results in the mean SSD,  $\mu_s \approx 42.46$  cm with the corresponding SSD standard deviation,  $\sigma_s \approx 0.49$  cm. As the SPA measured SSD at 06:22 hrs IST, January 8, 2016, is 54.9 cm, so  $\mu_s$  is underestimated. Naturally, the mean SSWE,  $\mu_{ss} \approx 133.76$  mm (with SSWE standard deviation,  $\sigma_{ss} \approx 1.53$  mm) is also lower compared to the SPA measured SSWE of 173 mm. Thus, to effectively optimise the volumetric height,  $\eta$  needs to be suitably increased (Cloude, 2005, 2010).

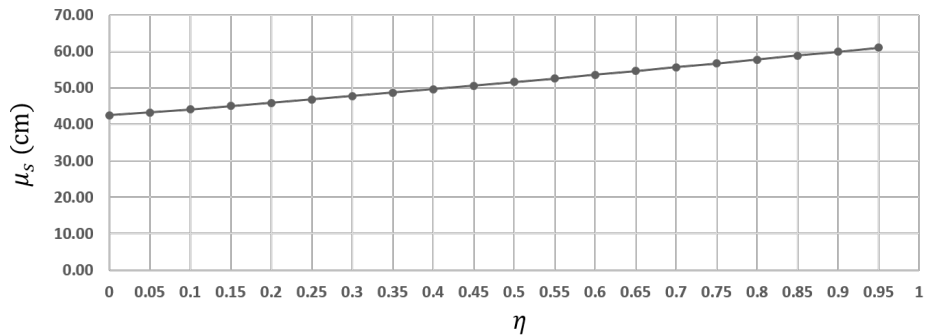


Figure 4.7: Increasing mean SSD with respect to the scaling parameter  $\eta$ .

In this context, Cloude (2005) has suggested setting  $\eta = 0.4$  for which the accuracy of the estimated tree height is found to be more than 90%. Although by keeping  $\eta = 0.4$ ,  $\mu_s \approx 49.64$  cm ( $\sigma_s \approx 0.54$  cm) is obtained with  $\sim 90.42\%$  accuracy, the complexity of the snow microstructure, anisotropy, and length scales necessitates the need for achieving even higher accuracies (Leinss et al., 2016). Moreover, in the presence of significantly varying hydrometeorological conditions which include high surface roughness and associated uncertainty sources (section 4.1), the volume and surface coherence amplitudes generally do not reach expected values of higher than 0.8 (Cloude, 2005; Kugler et al., 2015). Therefore, with  $\eta = 0.65$ , the best SSD and SSWE accuracies of 99.53% ( $\mu_s \approx$



54.64 cm) and 99.48% ( $\mu_{ss} \approx 172.10$  mm) respectively are achieved over Dhundi with low standard deviations ( $\sigma_s \approx 0.58$  cm,  $\sigma_{ss} \approx 1.82$  mm) accounting for high reliability. These results highlight the significance of this scaling parameter  $\eta$  towards controlling the snow structural height variations (Cloude, 2005, 2010) and hence, the robustness of the hybrid DEM differencing model (section 2.3) is verified.

#### *Computing sinc Inverse*

In order to test the accuracy of the  $\text{sinc}_\pi$  inverse function, sample test data representing the actual inverse,  $\alpha_r$ , have been prepared as shown in Table 4.1. Next, the  $\text{sinc}_\pi$  of these data,  $\text{sinc}_\pi(\alpha_r)$ , is computed which essentially corresponds to the possible  $\gamma(\vec{w}_v)$  values. So, the idea of performing SA in this scenario is to check the accuracy of the calculated  $\text{sinc}_{\pi_C}^{-1}$  (Eq. (2.11c)) and  $\text{sinc}_{\pi_S}^{-1}$  (Eq. (2.11b)) of the  $\text{sinc}_\pi(\alpha_r)$  values by comparing these with  $\alpha_r$ .

Table 4.1: Comparison between the normalised Cloude (2010) sinc inverse and the secant sinc inverse methods.

| $\alpha_r$ (rad) | $\text{sinc}_\pi(\alpha_r)$ | $\text{sinc}_{\pi_C}^{-1}$ (rad) | $\text{sinc}_{\pi_S}^{-1}$ (rad) |
|------------------|-----------------------------|----------------------------------|----------------------------------|
| 0.1              | 0.984                       | 0.103                            | 0.100                            |
| 0.2              | 0.935                       | 0.206                            | 0.200                            |
| 0.3              | 0.858                       | 0.308                            | 0.300                            |
| 0.4              | 0.757                       | 0.409                            | 0.400                            |
| 0.5              | 0.637                       | 0.509                            | 0.500                            |
| 0.6              | 0.505                       | 0.607                            | 0.600                            |
| 0.7              | 0.368                       | 0.703                            | 0.700                            |
| 0.8              | 0.234                       | 0.798                            | 0.800                            |
| 0.9              | 0.109                       | 0.891                            | 0.900                            |

From Table 4.1 it is observed that the secant method converges exactly (up to 13 decimal places) to the actual  $\alpha_r$ , while the normalised Cloude (2010) approximation of the  $\text{sinc}_\pi$  inverse has some minute errors involved (RMSE  $\approx 0.02$  rad). Similarly, the sinc function is tested (Table 4.2) where  $\text{sinc}_C^{-1}$  and

$\text{sinc}_S^{-1}$  denote the standard [Cloude \(2010\)](#) approximation (Eq. (2.11a)) and  
 605 the secant method of root finding for the traditional sinc function respectively. Again, the secant method exactly converges (up to 13 decimal places) whereas RMSE  $\approx 0.02$  rad is associated with the  $\text{sinc}_C^{-1}$ . Here, the computed results shown in [Table 4.1](#) and [Table 4.2](#) are rounded to 3 decimal places.

Table 4.2: Comparison between the traditional [Cloude \(2010\)](#) sinc inverse and the secant sinc inverse methods.

| $\alpha_r$ (rad) | $\text{sinc}(\alpha_r)$ | $\text{sinc}_C^{-1}$ (rad) | $\text{sinc}_S^{-1}$ (rad) |
|------------------|-------------------------|----------------------------|----------------------------|
| 0.1              | 0.998                   | 0.103                      | 0.100                      |
| 0.2              | 0.993                   | 0.207                      | 0.200                      |
| 0.3              | 0.985                   | 0.310                      | 0.300                      |
| 0.4              | 0.974                   | 0.413                      | 0.400                      |
| 0.5              | 0.959                   | 0.516                      | 0.500                      |
| 0.6              | 0.941                   | 0.618                      | 0.600                      |
| 0.7              | 0.920                   | 0.721                      | 0.700                      |
| 0.8              | 0.897                   | 0.823                      | 0.800                      |
| 0.9              | 0.870                   | 0.925                      | 0.900                      |

Therefore, by performing the SA of the  $\text{sinc}_{\pi_C}^{-1}$ ,  $\text{sinc}_{\pi_S}^{-1}$ ,  $\text{sinc}_C^{-1}$ , and  $\text{sinc}_S^{-1}$ , it  
 610 is clearly understood that the secant method provides highly accurate results. Hence, in this work,  $\text{sinc}_{\pi_S}^{-1}$  is applied for solving Eq. (2.9a) wherein the  $\text{sinc}_{\pi_C}^{-1}(\gamma(\vec{w}_v))$  value is used as an initial guess to the secant method for faster convergence.

#### *SSD Ensemble Window*

615 Another essential free parameter used in the Pol-InSAR based SSD estimation model (section 2.3) is the SSD ensemble averaging window size. By keeping  $\eta = 0.65$ ,  $\eta' = 5$ , and other ensemble window sizes constant, the SA has been carried out to observe the SSD variations which are shown in [Figure 4.8](#). Here, the ensemble windows are the same which have been previously applied

620 for the FSD values (section 4.2.1) so as to appropriately compare the SSD and FSD estimates.

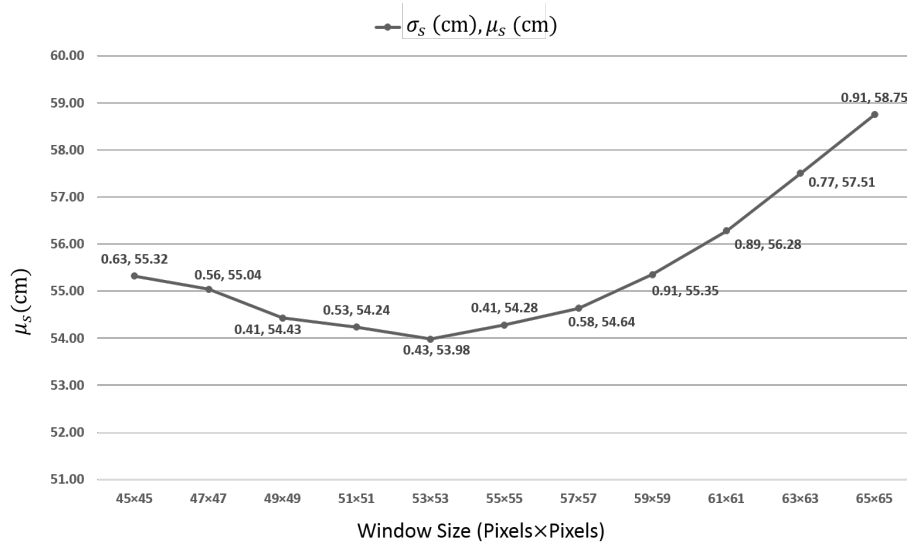


Figure 4.8: Effect of the ensemble window size on the SSD values.

The graphical representation in Figure 4.8 shows that when the window size is increased beyond  $57 \times 57$ , the SSD values increase sharply whereas, between the windows  $53 \times 53$  and  $57 \times 57$ , the values are mostly similar. This could be attributed by the fact that, in mountainous terrains, elevation, and not distance, plays a critical role in controlling the snow accumulation (Liu et al., 2017; Singh et al., 2014, 2017; Thakur et al., 2012). The varying topographical conditions prominently visible in Figure 3.2 also ascertain that for larger window sizes, the snow depth variability could increase if a nearby mountain also lies within the neighbourhood window. So, considering these aspects, the ensemble window size of  $57 \times 57$  is selected which results in  $\mu_s \approx 54.64$  cm with  $\sigma_s \approx 0.58$  cm as discussed in the scaling parameter SA.

#### 4.2.3. DEM and LIA Error Analysis

During the field visit (section 3.1.2), several DGPS points which had been acquired are used to check the accuracy of the ALOS PALSAR DEM. In essence,

the observed errors are then used to analyse the change in the LIA (Eq. (2.12)) induced by the corrected DEM (the erroneous DEM pixels are replaced by the respective DGPS measurements).

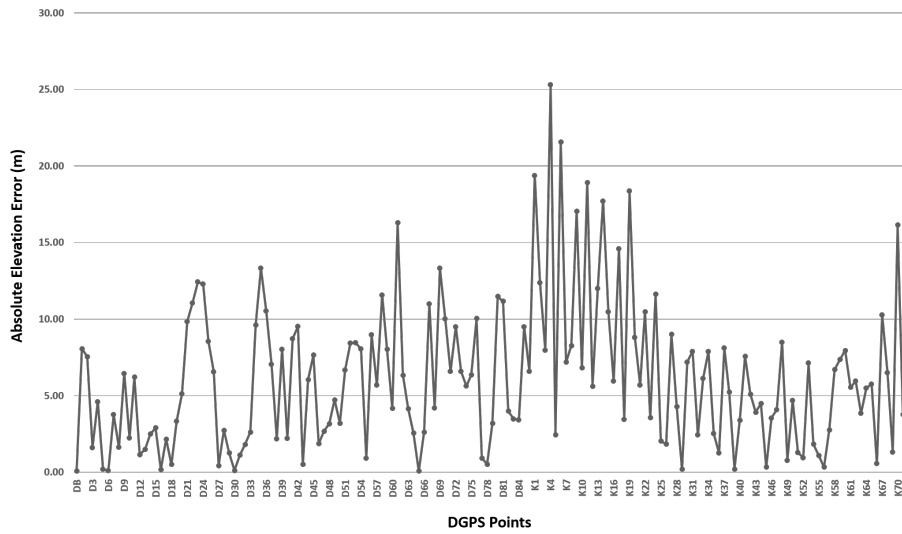
The DEM errors calculated using the Dhundi and Kothi DGPS readings are displayed in Figure 4.9(a) and the subsequent LIA differences (computed from the corrected and original DEMs) for these points are shown in Figure 4.9(b). As seen from these graphs, the absolute elevation errors range from 0.08 m to 16.30 m in the Dhundi region, whereas these vary from 0.19 m to 25.32 m in the Kothi area. Accordingly, the RMSE values for the elevation errors are approximately 6.71 m and 8.8 m respectively.

In addition, the LIA varies from  $0^\circ$  to  $7.59^\circ$  (Dhundi) and  $0^\circ$  to  $0.17^\circ$  (Kothi) in these areas with the corresponding RMSE being nearly  $2.54^\circ$  and  $0.02^\circ$ . However, since the LIA is dependent on the slope values (Eq. (2.12)), the DEM errors do not significantly influence the LIA. Also, in the FSD inversion model and the vertical wavenumber calculation (used in the SSD estimation) given by Eq. (2.7) and Eq. (2.9b) respectively, the sine (sin) of the LIA is considered. So, the minute changes in the LIA do not strongly affect the FSD and SSD estimates which are obtained after applying sufficient ensemble averaging operation (section 2). Evidently, the LIA only changes by about  $1.9^\circ$  near the Dhundi base station and thus, the FSD and SSD results are not exhibiting any sizeable impact from the associated DEM errors.

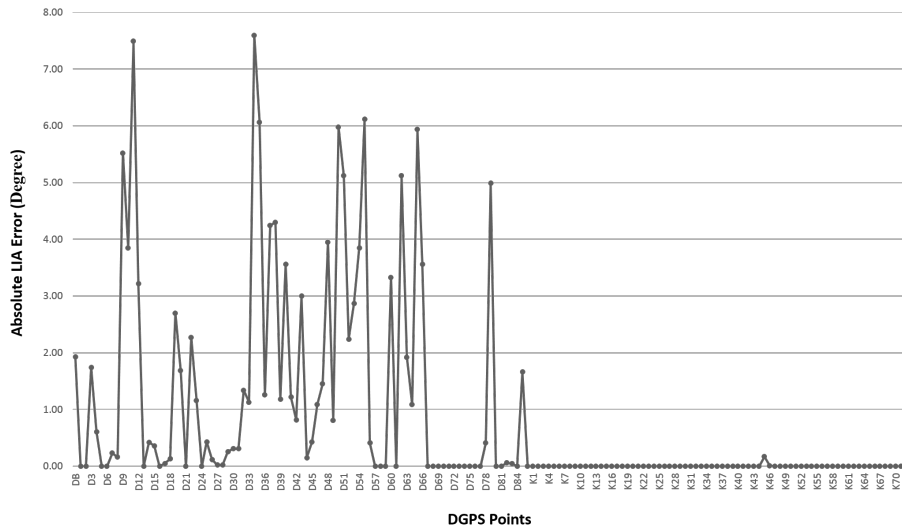
Therefore, the SA concerning the DEM errors and its propagation highlights that the subsequent LIA errors are not directly governed by the changes in the elevation values, rather the slopes in  $x$  and  $y$  directions (section 2.4.3) act as the primary error sources. Also, the ALOS PALSAR DEM is sufficiently accurate even in the complex terrains and hence, its usage in the LIA computation is justified.

#### *4.3. Comparative Analysis of the Estimates*

In order to visually observe the spatial patterns of the FSD and SSD estimates, suitable maps have been prepared which are shown in Figure 4.10(a)



(a)



(b)

Figure 4.9: (a) Absolute DEM errors obtained by comparing ALOS PALSAR DEM and the DGPS measurements and (b) observed absolute LIA errors. Here DB is the Dhundi base station point, D1-D86 are acquired in the Dhundi region, and K1-K72 are measured in the Kothi area using the DGPS.

and Figure 4.10(b) respectively. Here, the resultant FSWE and SSWE maps are not shown as these have been computed by multiplying the constant snow densities,  $\rho_f = 0.07 \text{ g/cm}^3$  and  $\rho_s = 0.315 \text{ g/cm}^3$  to the FSD and SSD values respectively. Therefore, they have similar spatial characteristics like those of the snow depth maps.

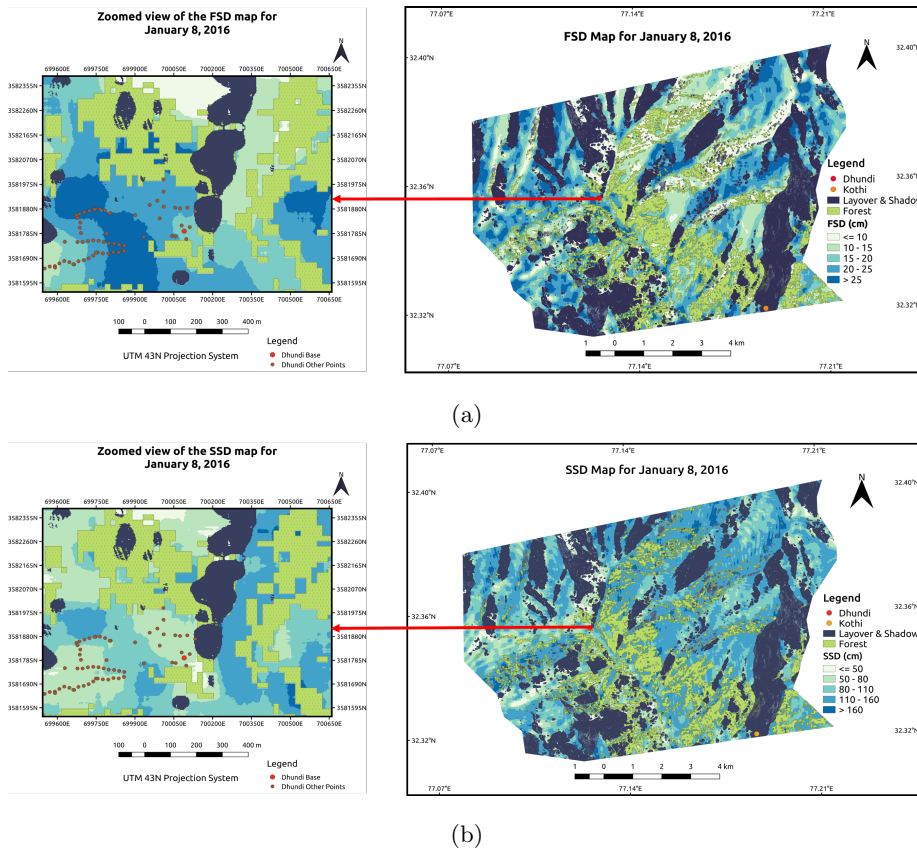


Figure 4.10: Zoomed views of the (a) FSD map and (b) SSD map for January 8, 2016. Here, the ground points surveyed (section 3.1.2) are shown wherein the closely spaced points have been acquired using the DGPS kinematic mode and fall on the nearby roads in the Dhundi region. The other points including the Dhundi base are measured using the static mode. Since the Kothi area falls in the layover and shadow zone, it is excluded from the zoomed view analysis.

As discussed earlier in sections 4.2.1 and 4.2.2, the optimal FSD and SSD

ensemble window sizes are  $65 \times 65$  and  $57 \times 57$  respectively. The maps in Figure 4.10 show these ensemble averaged estimates wherein  $\mu_f \approx 18.93 \pm 5.03$  cm ( $\sigma_f \approx 0.1$  cm) and  $\mu_s \approx 54.64 \pm 5.19$  cm ( $\sigma_s \approx 0.58$  cm) are observed over the  $3 \times 3$  neighbourhood window surrounding the Dhundi area with the corresponding  $\mu_{fs} \approx 13.25 \pm 5.02$  mm ( $\sigma_{fs} \approx 0.07$  mm) and  $\mu_{ss} \approx 172.10 \pm 5.61$  mm ( $\sigma_{ss} \approx 1.82$  mm). Here, the uncertainties are calculated based on the standard error of the estimate and the SPA measurement biases of 5 cm and 5 mm for the SD and SWE have been assumed respectively.

In addition, the overall mean FSD and SSD are 17.90 cm and 112.17 cm respectively wherein the standard deviations are found to be  $\sim 6.46$  cm and  $\sim 30.80$  cm. Accordingly, the mean FSWE and SSWE are  $\sim 12.12$  mm and  $\sim 377.81$  mm respectively where the associated standard deviations are  $\sim 4.46$  mm and  $\sim 101.55$  mm.

The high SSD and SSWE standard deviations for the complete region highlight the extreme topographical conditions present in the study area. These variations can be confirmed from the ground survey (section 3.1.2) where the points (shown in Figure 4.10) had been acquired by considering the terrain undulations. Also, the aspect, slope, and elevation significantly influence the FSD and SSD estimates, the details of which have been discussed in the previous section.

Apart from this, it can be observed that these estimates are lower in the Dhundi base station area as compared to the surrounding regions. This phenomenon can be attributed to the presence of the human settlements (Figure 3.2(b)) near the base point and are expected to have less snow accumulation than the natural surroundings. Moreover, the effect of multiple or double bounce scattering (Z4) near the Dhundi base is prominent even during the winter (Figure 4.1(a)). So, this could effectively reduce the copolar, volume and surface coherences (sections 4.2.1 and 4.2.2) thereby explaining this observation.

## 700 **5. Conclusion and Future Scope**

The primary focus of this research lies in estimating the snow depth using which the snow water equivalent has been measured. Here, two different types of snow have been considered freshly fallen (new) snow and standing (old) snow. In order to compute the FSD, the CPD method has been applied (section 2.2) on the January 8, 2016, TSX-TDX CoSSC bistatic dataset acquired over the 705 Beas watershed, northwestern Himalayas (section 3). Additionally, the hybrid DEM differencing and coherence amplitude inversion algorithm based on the single-baseline Pol-InSAR technique has been utilised to estimate the SSD for the same dataset (section 2.3). Also, the corresponding FSWE and SSWE are 710 obtained by multiplying constant fresh and standing snow densities.

Due to the complex hydrometeorological and topographical conditions of the study area (section 3.1.1), significant uncertainty sources are present. These include the forests, boulders, highly rough surfaces, and human settlements (Figure 3.2) which substantially reduce the surface and volume scattering 715 coherences required to estimate the snow depths with adequate accuracy (2.4). Moreover, the limited ground-truth data availability has always been a major challenge from the onset of this work (section 3.2). Apart from this, the SAR data are affected by layover, shadowing and foreshortening in mountainous terrains and hence, these errors are inherently propagated through 720 the subsequent processing steps. Furthermore, the PolSAR and Pol-InSAR models involve several user-defined parameters which have to be optimised (section 2). In short, these are the main concerns involved in this work which are addressed by means of identifying the potential uncertainty sources ( $H/\alpha$  decomposition and Wishart classification) and performing appropriate 725 sensitivity analysis (section 2.4.3).

Thus, the novelty of this research lies in suitably modifying and ultimately improving the hybrid Pol-InSAR model (section 2.3) to estimate the SSD which is new in the context of cryospheric studies. Additionally, the PolSAR CPD method for FSD retrieval has been tested for the first time in the presence



730 of extreme topographically varying conditions. Although the FSD and SSD ground-truth measurements from only the Dhundi station had been available, the high accuracies of 94.83% and 99.53% respectively imply that these improved models work sufficiently well under the complex hydrometeorological situations.

As part of future work, it is recommended to use the multi-baseline Pol-  
735 InSAR technique (Cloude, 2010) wherein  $k_z$  can be simulated (instead of scaling by  $\eta'$ ) after an appropriate accuracy assessment (Kumar et al., 2017). Similarly, the effect of different window shapes (square or rectangular) and sizes can be considered for the ensemble averaging operation. This sort of sensitivity analysis will help in deciding optimal window structures separately for each model.  
740 Moreover, it is recommended to apply scattering mechanism based masks in conjunction with snow masks prepared from the high resolution optical datasets such as those provided by Sentinel-2 (Zhu et al., 2015). Additionally, the prior classification of the dry and wet snow including the preparation of snow cover maps (Leinss et al., 2018; Thakur et al., 2012; Zhu et al., 2015) as necessary  
745 preprocessing steps will certainly improve the uncertainty assessment process.

Also, the use of the newer multi-temporal high resolution L-band datasets acquired by the upcoming SAR missions (Tridon et al., 2018; Rosen et al., 2017) is recommended to further verify and validate these models. Moreover, radar altimeters such as the Ka-band InSAR altimeter could potentially improve the  
750 SD and SWE estimates, and could also be used for operational snow depth monitoring on a large-scale (Hensley et al., 2016; Kim et al., 2018; Moller et al., 2011; Speziali et al., 2018).

In this work, one dataset (January 8, 2016) was used for analysis. Preferably, if a full scale time series analysis is performed, then the robustness of the SSD  
755 and FSD retrieval models can be checked. Furthermore, Pol-InSAR coherency optimisation can be carried out to suitably adjust the scattering phase centres (Cloude, 2005, 2010). Moreover, the snow densities need to be computed gridwise (or if possible, pixelwise) by using hydrological modelling approaches (Bartelt & Lehning, 2002; Liang et al., 1994). These can also be estimated from  
760 the PolSAR based techniques which are in practice (Singh et al., 2017; Thakur

et al., 2012). Finally, appropriate statistical significance testing needs to be carried out to quantify further the uncertainties associated with the FSD and SSD estimates.

### Acknowledgements

765 This research work was carried out as part of the ISRO EOAM mountain ecosystem, TANDEM-X AO and ALOS-RA4 project (EOAM-ME (WRD)) on the Himalayan glaciers. Also, this work was conducted within the IIRS, ISRO and University of Twente, Faculty ITC joint education programme (JEP) framework. The authors are grateful to IIRS, ISRO, University of  
770 Twente, Faculty ITC along with SASE, DRDO and the FOSS4G community for providing the necessary means to conduct this study.

### References

- Abe, T., Yamaguchi, Y., & Sengoku, M. (1990). Experimental study of microwave transmission in snowpack. *IEEE Trans. Geosci. Remote Sens.*,  
775 *28*, 915–921. doi:[10.1109/36.58981](https://doi.org/10.1109/36.58981).
- Balss, U., Breit, H., Duque, S., Fritz, T., & Rossi, C. (2012). *CoSSC Generation and Interferometric Considerations (TD-PGS-TN-3129)*. Technical Report Remote Sensing Technology Institute, DLR Oberpfaffenhofen, Germany. URL: [https://tandemx-science.dlr.de/pdfs/TD-PGS-TN-3129\\_](https://tandemx-science.dlr.de/pdfs/TD-PGS-TN-3129_CoSSCGenerationInterferometricConsiderations_1.0.pdf)  
780 [CoSSCGenerationInterferometricConsiderations\\_1.0.pdf](https://tandemx-science.dlr.de/pdfs/TD-PGS-TN-3129_CoSSCGenerationInterferometricConsiderations_1.0.pdf).
- Bartelt, P., & Lehning, M. (2002). A physical SNOWPACK model for the Swiss avalanche warning. *Cold Reg. Sci. Technol.*, *35*, 123–145. doi:[10.1016/S0165-232X\(02\)00074-5](https://doi.org/10.1016/S0165-232X(02)00074-5).
- Brunner, D. (2009). *Advanced Methods For Building Information Extraction From Very High Resolution SAR Data To Support Emergency Response*.  
785 Doctoral thesis Trento: University of Trento. URL: [http://eprints-phd.biblio.unitn.it/233/1/PHD\\_Thesis\\_Dominik\\_Brunner.pdf](http://eprints-phd.biblio.unitn.it/233/1/PHD_Thesis_Dominik_Brunner.pdf).

- Cheney, E. W., & Kincaid, D. R. (2012). Nonlinear equations. In *Numer. Math. Comput.* (pp. 114–150). Boston, USA: Cengage Learning. (7th ed.).
- 790 Cloude, S. R. (2005). *POL-InSAR training course*. Technical Report ESA. URL: [https://earth.esa.int/landtraining07/pol-insar\\_training\\_course.pdf](https://earth.esa.int/landtraining07/pol-insar_training_course.pdf).
- Cloude, S. R. (2010). *Polarisation: Applications in Remote Sensing*. New York: Oxford University Press. doi:[10.1093/acprof:oso/9780199569731.001.0001](https://doi.org/10.1093/acprof:oso/9780199569731.001.0001).
- 795 Conde, V., Nico, G., Mateus, P., Catalão, J., Kontu, A., & Gritsevich, M. (2019). On The Estimation of Temporal Changes of Snow Water Equivalent by Spaceborne Sar Interferometry: A New Application for the Sentinel-1 Mission. *J. Hydrol. Hydromechanics*, *67*. doi:[10.2478/johh-2018-0003](https://doi.org/10.2478/johh-2018-0003).
- 800 Deems, J. S., Painter, T. H., & Finnegan, D. C. (2013). Lidar measurement of snow depth: a review. *J. Glaciol.*, *59*, 467–479. doi:[10.3189/2013JoG12J154](https://doi.org/10.3189/2013JoG12J154).
- ESA (2018). SNAP. URL: <http://step.esa.int/main/toolboxes/snap/>.
- Guneriussen, T., Høgda, K. A., Johnsen, H., & Lauknes, I. (2001). InSAR for estimation of changes in snow water equivalent of dry snow. *IEEE Trans. Geosci. Remote Sens.*, *39*, 2101–2108. doi:[10.1109/36.957273](https://doi.org/10.1109/36.957273).
- 805 Hajnsek, I., Kugler, F., Lee, S.-K., & Papathanassiou, K. P. (2009). Tropical-Forest-Parameter Estimation by Means of Pol-InSAR: The INDREX-II Campaign. *IEEE Trans. Geosci. Remote Sens.*, *47*, 481–493. doi:[10.1109/TGRS.2008.2009437](https://doi.org/10.1109/TGRS.2008.2009437).
- 810 Hanssen, R. F. (2001). *Radar Interferometry - Data Interpretation and Error Analysis* volume 2 of *Remote Sensing and Digital Image Processing*. Dordrecht: Kluwer Academic Publishers. doi:[10.1007/0-306-47633-9](https://doi.org/10.1007/0-306-47633-9).
- Hensley, S., Moller, D., Oveisgharan, S., Michel, T., & Wu, X. (2016). Ka-Band Mapping and Measurements of Interferometric Penetration of the Greenland

- 815 Ice Sheets by the GLISTIN Radar. *IEEE J. Sel. Top. Appl. Earth Obs. Remote Sens.*, 9, 2436–2450. doi:10.1109/JSTARS.2016.2560626.
- Hoehn, E. W., & Zebker, H. (2000). Penetration depths inferred from interferometric volume decorrelation observed over the Greenland Ice Sheet. *IEEE Trans. Geosci. Remote Sens.*, 38, 2571–2583. doi:10.1109/36.885204.
- 820 JetBrains (2018). PyCharm Documentation. URL: <https://www.jetbrains.com/pycharm/documentation/index.html>.
- Jones, E., Oliphant, E., & Peterson, P. (2001). SciPy: Open Source Scientific Tools for Python. URL: <http://www.scipy.org/>.
- Kim, E. J., Gatebe, C. K., Hall, D. K., & Kang, D. H. (2018). *NASA's SnowEx Campaign and Measuring Global Snow from Space (GSFC-E-DAA-TN55784)*.  
825 Technical Report NASA Pyeongchang, Republic of Korea. URL: <https://ntrs.nasa.gov/search.jsp?R=20180005187>.
- Kugler, F., Lee, S.-K., Hajnsek, I., & Papathanassiou, K. P. (2015). Forest Height Estimation by Means of Pol-InSAR Data Inversion: The Role of the  
830 Vertical Wavenumber. *IEEE Trans. Geosci. Remote Sens.*, 53, 5294–5311. doi:10.1109/TGRS.2015.2420996.
- Kumar, S., Khati, U. G., Chandola, S., Agrawal, S., & Kushwaha, S. P. (2017). Polarimetric SAR Interferometry based modeling for tree height and aboveground biomass retrieval in a tropical deciduous forest. *Adv. Sp. Res.*,  
835 60, 571–586. doi:10.1016/j.asr.2017.04.018.
- Kumar, V., & Venkataraman, G. (2011). SAR interferometric coherence analysis for snow cover mapping in the western Himalayan region. *Int. J. Digit. Earth*, 4, 78–90. doi:10.1080/17538940903521591.
- Lee, J.-S., & Pottier, E. (2009). *Polarimetric Radar Imaging: From Basics to*  
840 *Applications*. Boca Raton, Florida, USA: CRC Press. URL: <https://www.taylorfrancis.com/books/9781420054972>.

- Lee, J.-S., Schuler, D. L., & Ainsworth, T. L. (2000). Polarimetric SAR data compensation for terrain azimuth slope variation. *IEEE Trans. Geosci. Remote Sens.*, *38*, 2153–2163. doi:[10.1109/36.868874](#).
- 845 Leica Geosystems AG (2012). *Leica GS10/GS15 User Manual (772916-4.1.0en)*. Technical Report Leica Geosystems AG Heerbrugg, Switzerland. URL: [http://www.surveyequipment.com/PDFs/Leica\\_Viva\\_GS10\\_GS15\\_User\\_Manual.pdf](http://www.surveyequipment.com/PDFs/Leica_Viva_GS10_GS15_User_Manual.pdf).
- Leinss, S., Antropov, O., Vehvilainen, J., Lemmetyinen, J., Hajnsek, I., & 850 Praks, J. (2018). Wet Snow Depth from Tandem-X Single-Pass Insar Dem Differencing. In *IGARSS 2018 - 2018 IEEE Int. Geosci. Remote Sens. Symp.* (pp. 8500–8503). IEEE. doi:[10.1109/IGARSS.2018.8518661](#).
- Leinss, S., Löwe, H., Proksch, M., Lemmetyinen, J., Wiesmann, A., & Hajnsek, I. (2016). Anisotropy of seasonal snow measured by polarimetric 855 phase differences in radar time series. *The Cryosphere*, *10*, 1771–1797. doi:[10.5194/tc-10-1771-2016](#).
- Leinss, S., Parrella, G., & Hajnsek, I. (2014). Snow height determination by polarimetric phase differences in X-Band SAR Data. *IEEE J. Sel. Top. Appl. Earth Obs. Remote Sens.*, *7*, 3794–3810. doi:[10.1109/JSTARS.2014.2323199](#).
- 860 Leinss, S., Wiesmann, A., Lemmetyinen, J., & Hajnsek, I. (2015). Snow Water Equivalent of Dry Snow Measured by Differential Interferometry. *IEEE J. Sel. Top. Appl. Earth Obs. Remote Sens.*, *8*, 3773–3790. doi:[10.1109/JSTARS.2015.2432031](#).
- Li, H., Wang, Z., He, G., & Man, W. (2017). Estimating Snow Depth and Snow 865 Water Equivalence Using Repeat-Pass Interferometric SAR in the Northern Piedmont Region of the Tianshan Mountains. *J. Sensors*, *2017*, 1–17. doi:[10.1155/2017/8739598](#).
- Liang, X., Lettenmaier, D. P., Wood, E. F., & Burges, S. J. (1994). A simple hydrologically based model of land surface water and energy fluxes

- 870 for general circulation models. *J. Geophys. Res.*, *99*, 14415–14428. doi:[10.1029/94JD00483](https://doi.org/10.1029/94JD00483).
- Liu, Y., Li, L., Yang, J., Chen, X., & Hao, J. (2017). Estimating snow depth using multi-source data fusion based on the D-InSAR method and 3DVAR fusion algorithm. *Remote Sens.*, *9*. doi:[10.3390/rs9111195](https://doi.org/10.3390/rs9111195).
- 875 Luo, X., Richter, B., & Cole, A. (2014). *GLONASS only and BeiDou only RTK Positioning*. Technical Report Leica Geosystems AG Heerbrugg, Switzerland. URL: [https://leica-geosystems.com/-/media/Files/LeicaGeosystems/Products/WhitePapers/GLONASS\\_BeiDou\\_RTK\\_Positioning\\_WPA.ashx](https://leica-geosystems.com/-/media/Files/LeicaGeosystems/Products/WhitePapers/GLONASS_BeiDou_RTK_Positioning_WPA.ashx).
- 880 Majumdar, S., Thakur, P. K., Chang, L., & Kumar, S. (2019). X-band Polarimetric SAR Copolar Phase Difference for Fresh Snow Depth Estimation in the Northwestern Himalayan Watershed. URL: <https://igarss2019.org/Papers/ViewPapers.asp?PaperNum=3115> accepted in 2019 IEEE International Geoscience and Remote Sensing Symposium (IGARSS 2019), Yokohama, Japan.
- 885 Moller, D., Hensley, S., Sadowy, G. A., Fisher, C. D., Michel, T., Zawadzki, M., & Rignot, E. (2011). The Glacier and Land Ice Surface Topography Interferometer: An Airborne Proof-of-Concept Demonstration of High-Precision Ka-Band Single-Pass Elevation Mapping. *IEEE Trans. Geosci. Remote Sens.*, *49*, 827–842. doi:[10.1109/TGRS.2010.2057254](https://doi.org/10.1109/TGRS.2010.2057254).
- 890 Moreira, A., Prats-Iraola, P., Younis, M., Krieger, G., Hajnsek, I., & Papathanassiou, K. P. (2013). A tutorial on synthetic aperture radar. *IEEE Geosci. Remote Sens. Mag.*, *1*, 6–43. doi:[10.1109/MGRS.2013.2248301](https://doi.org/10.1109/MGRS.2013.2248301).
- Papathanassiou, K., & Cloude, S. (2001). Single-baseline polarimetric SAR interferometry. *IEEE Trans. Geosci. Remote Sens.*, *39*, 2352–2363. doi:[10.1109/36.964971](https://doi.org/10.1109/36.964971).
- 895

- Parrella, G., Hajnsek, I., & Papathanassiou, K. P. (2013). On the Interpretation of L- and P-Band PolSAR Signatures of Polythermal Glaciers. In *6th Int. Work. Sci. Appl. SAR Polarim. Polarim. Interferom.* (pp. 1–6). Frascati, Italy. URL: [https://elib.dlr.de/78902/1/s7\\_parre.pdf](https://elib.dlr.de/78902/1/s7_parre.pdf).  
900
- PostgreSQL (2019). PostgreSQL. URL: <https://www.postgresql.org/>.
- QGIS (2016). Changelog for QGIS 2.18. URL: <https://www.qgis.org/en/site/forusers/visualchangelog218/index.html>.
- Reynolds, B. (1983). The chemical composition of snow at a rural upland site in Mid-wales. *Atmos. Environ.*, *17*, 1849–1851. doi:10.1016/0004-6981(83)90193-2.  
905
- Riche, F., Montagnat, M., & Schneebeli, M. (2013). Evolution of crystal orientation in snow during temperature gradient metamorphism. *J. Glaciol.*, *59*, 47–55. doi:10.3189/2013JoG12J116.
- Rosen, P., Hensley, S., Shaffer, S., Edelstein, W., Kim, Y., Kumar, R., Misra, T., Bhan, R., & Sagi, R. (2017). The NASA-ISRO SAR (NISAR) mission dual-band radar instrument preliminary design. In *2017 IEEE Int. Geosci. Remote Sens. Symp.* (pp. 3832–3835). IEEE. doi:10.1109/IGARSS.2017.8127836.  
910
- Sihvola, A. (1999). *Electromagnetic Mixing Formulas and Applications*. (1st ed.). UK: The Institution of Engineering and Technology. doi:10.1049/PBEW047E.  
915
- Singh, G., Venkataraman, G., Yamaguchi, Y., & Park, S.-E. (2014). Capability Assessment of Fully Polarimetric ALOSPALSAR Data for Discriminating Wet Snow From Other Scattering Types in Mountainous Regions. *IEEE Trans. Geosci. Remote Sens.*, *52*, 1177–1196. doi:10.1109/TGRS.2013.2248369.  
920
- Singh, G., Verma, A., Kumar, S., Snehamani, Ganju, A., Yamaguchi, Y., & Kulkarni, A. V. (2017). Snowpack Density Retrieval Using Fully Polarimetric TerraSAR-X Data in the Himalayas. *IEEE Trans. Geosci. Remote Sens.*, *55*, 6320–6329. doi:10.1109/TGRS.2017.2725979.

- 925 Snehmani, Venkataraman, G., Nigam, A. K., & Singh, G. (2010). Development of an inversion algorithm for dry snow density estimation and its application with ENVISAT-ASAR dual co-polarization data. *Geocarto Int.*, *25*, 597–616. doi:[10.1080/10106049.2010.516843](https://doi.org/10.1080/10106049.2010.516843).
- Speziali, F., Trampuz, C., Placidi, S., Hendriks, L. C. I., Ludwig, M., & Meta, A. 930 (2018). Development of the Multichannel Interferometric Ka-Band Airborne SAR Instrument (KaSAR). In *EUSAR 2018; 12th Eur. Conf. Synth. Aperture Radar* (pp. 1–5). Aachen, Germany. URL: <https://ieeexplore.ieee.org/abstract/document/8438262>.
- Takala, M., Luojus, K., Pulliainen, J., Derksen, C., Lemmetyinen, J., Kärnä, 935 J.-P., Koskinen, J., & Bojkov, B. (2011). Estimating northern hemisphere snow water equivalent for climate research through assimilation of space-borne radiometer data and ground-based measurements. *Remote Sens. Environ.*, *115*, 3517–3529. doi:[10.1016/j.rse.2011.08.014](https://doi.org/10.1016/j.rse.2011.08.014).
- Tedesco, M. (Ed.) (2015). *Remote Sensing of the Cryosphere*. Chichester, UK: 940 John Wiley & Sons, Ltd. doi:[10.1002/9781118368909](https://doi.org/10.1002/9781118368909).
- Thakur, P. K., Aggarwal, S., Garg, P., Garg, R., Mani, S., Pandit, A., & Kumar, S. (2012). Snow physical parameters estimation using space-based Synthetic Aperture Radar. *Geocarto Int.*, *27*, 263–288. doi:[10.1080/10106049.2012.672477](https://doi.org/10.1080/10106049.2012.672477).
- 945 Thakur, P. K., Aggarwal, S. P., Arun, G., Sood, S., Senthil Kumar, A., Mani, S., & Dobhal, D. P. (2017). Estimation of Snow Cover Area, Snow Physical Properties and Glacier Classification in Parts of Western Himalayas Using C-Band SAR Data. *J. Indian Soc. Remote Sens.*, *45*, 525–539. doi:[10.1007/s12524-016-0609-y](https://doi.org/10.1007/s12524-016-0609-y).
- 950 Tridon, D. B., Sica, F., De Zan, F., Bachmann, M., & Krieger, G. (2018). Observation Strategy and Flight Configuration for Monitoring Earth Dynamics with the Tandem-L Mission. In *IGARSS 2018 - 2018 IEEE*



*International Geoscience and Remote Sensing Symposium* (pp. 5651–5654).  
doi:[10.1109/IGARSS.2018.8517757](https://doi.org/10.1109/IGARSS.2018.8517757).

955 Ulaby, F., Stiles, W., Dellwig, L., & Hanson, B. (1977). Experiments on the  
Radar Backscatter of Snow. *IEEE Trans. Geosci. Electron.*, *15*, 185–189.  
doi:[10.1109/TGE.1977.294490](https://doi.org/10.1109/TGE.1977.294490).

Usami, N., Muhuri, A., Bhattacharya, A., & Hirose, A. (2016). PolSAR Wet  
Snow Mapping With Incidence Angle Information. *IEEE Geosci. Remote*  
960 *Sens. Lett.*, *13*, 2029–2033. doi:[10.1109/LGRS.2016.2621891](https://doi.org/10.1109/LGRS.2016.2621891).

Wu, S., Li, J., & Huang, G. H. (2008). A study on DEM-derived primary  
topographic attributes for hydrologic applications: Sensitivity to elevation  
data resolution. *Appl. Geogr.*, *28*, 210–223. doi:[10.1016/j.apgeog.2008.  
02.006](https://doi.org/10.1016/j.apgeog.2008.02.006).

965 Yueh, S., Dinardo, S., Akgiray, A., West, R., Cline, D., & Elder, K. (2009).  
Airborne Ku-Band Polarimetric Radar Remote Sensing of Terrestrial Snow  
Cover. *IEEE Trans. Geosci. Remote Sens.*, *47*, 3347–3364. doi:[10.1109/  
TGRS.2009.2022945](https://doi.org/10.1109/TGRS.2009.2022945).

Zhu, Z., Wang, S., & Woodcock, C. E. (2015). Improvement and expansion of  
970 the Fmask algorithm: cloud, cloud shadow, and snow detection for Landsats  
47, 8, and Sentinel 2 images. *Remote Sens. Environ.*, *159*, 269–277. doi:[10.  
1016/j.rse.2014.12.014](https://doi.org/10.1016/j.rse.2014.12.014).

Zuniga, M., Habashy, T., & Kong, J. (1979). Active Remote Sensing of Layered  
Random Media. *IEEE Trans. Geosci. Electron.*, *17*, 296–302. doi:[10.1109/  
975 TGE.1979.294658](https://doi.org/10.1109/TGE.1979.294658).